A LATERAL FLOW SMART PHONE IMAGE ANALYSIS DIAGNOSTIC

A Thesis

presented to

the Faculty of California Polytechnic State University,

San Luis Obispo

In Partial Fulfillment

of the Requirements for the Degree

Master of Science in Biomedical Engineering

by

Christina Holly Tyrrell

August 2013

COMMITTEE MEMBERSHIP

TITLE:	A Lateral Flow Smart Phone Image Analysis Diagnostic
AUTHOR:	Christina Holly Tyrrell
DATE SUBMITTED:	August 2013
COMMITTEE CHAIR:	David Clague, Ph.D. Associate Professor, Biomedical Engineering California Polytechnic State University
COMMITTEE MEMBER:	Richard Savage, Ph.D. Associate Professor, Materials Engineering California Polytechnic State University
COMMITTEE MEMBER	Scott Hazelwood, Ph.D. Associate Professor, Biomedical Engineering California Polytechnic State University

ABSTRACT

A Lateral Flow Smart Phone Image Analysis Diagnostic

Christina Holly Tyrrell

A low cost compact diagnostic has many implications in today's society. Smart phone technology has exponentially grown and with it the imaging capabilities associated with smart phones. The goals of this research are i) to determine the feasibility of combining in the field smart phone images with color dependent assay results, ii) to develop a MatLab® image analysis code to analyze these results, and iii) compare limits of detection between the un-aided eye and MatLab® image analysis software.

Orange G dye is used to create a stock solution and subsequent titers for analysis. Autocad is used to design an assay platform of 10x10 wells that are printed via a Xerox® Phaser printer with wax ink onto nitrocellulose paper. Dilutions are performed and pipetted into the wells. The image analysis code is used to determine hue, saturation, and value (HSV) values of wells. A limit of detection study using the dye is performed. HSV values are used to form calibration curves. The resulting curve fit equations are then integrated into the image analysis code to determine dye concentration. Finally, the complete capability is demonstrated by using an analogous 10x10 well experimental nitrocellulose sheet, which included a follow-up experiment via a spot check analysis.

This study illustrates the feasibility of a low cost image analysis as a tool for lateral flow assay diagnostic versus the unaided eye. Future work includes using this protocol in conjunction with a lateral flow immunoassay and developing an application for the analysis.

VISUAL ABSTRACT

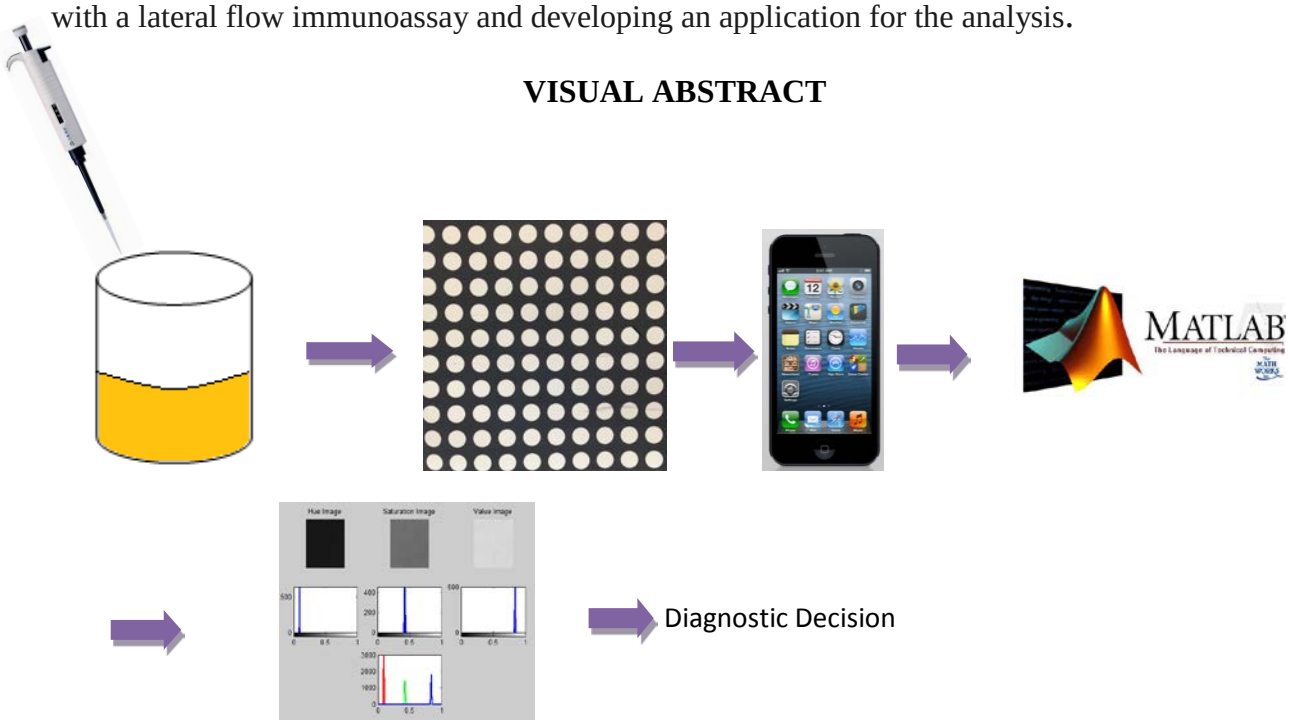

Keywords: Lateral flow assay (LFA), Colloidal gold, Organe G Dye, Gold nanoparticle (NP), Smart phone, Image analysis code.

ACKNOWLEDGMENTS

First I would like to thank my thesis advisor, Professor David Clague, for giving me the opportunity to work with him in the microfluidics laboratory and entrusting this project to me. He helped me tremendously when the project became difficult and it felt as though I would never finish, he was there to help me push through and to celebrate the successes. I thank him for all of the advice and effort he gave me.

I would also like to thank my committee members, Professors R. Savage and S. Hazelwood for graciously taking the time to review my work and attend my defense.

Without my Mom I would not have been able to accomplish all that I have. I would like to thank her for always being there for me to share my success, stress, love, and every other emotion. Without you Mom, I would not be the person I am today. You are truly the most amazing woman in the world and daily continue to inspire me. I would also like to thank my Aunt Amy and Sister Stephanie for always lovingly supporting me.

Last, but not least I would like to thank my husband, Michael Tyrrell for always being there to encourage me. He has stuck by my side during the most stressful time of my life and always went above and beyond to help me reach my goals. Thank you for taking this adventure with me, I love you!

To all of my family and friends who have been a part of this process, thank you so much. Without all of your love and support, I would not have been able to accomplish this.

Table of Contents

LIST OF TABLES

LIST OF FIGURES

1. INTRODUCTION

1.1 Lateral Flow Assay

The typical lateral flow assay (LFA) consists of three main parts; the surface layer, detection zone, and absorbent pad. The surface layer carries the sample from the application point along the strip to the detection zone. The detection zone contains the recognition elements. Lastly, the absorbent pad collects the remaining solute [1]. When antibodies are used as the recognition elements the LFA is referred to as a lateral flow immunoassay (LFIA) [1]. When a colloidal gold particle is coated with an antibody and combined with the corresponding antigen the immunoreactant is visually detected via a color change [2]. The main benefits of a LFA are; results are obtained quickly, they have long term stability, and they are inexpensive to manufacture [2]. The most familiar example of a LFA is the pregnancy test [1].

Colloidal gold immunoassays have become a popular topic in scientific research and have been developed by many laboratories. Some examples of uses are in the detection of hormones, viruses, and bacteria. An assay can be specifically designed to detect if a marker is present in a sample. If the marker is not present the antibody will accumulate on the membrane. There, the antibodies will be trapped by the conjugate while the sample flows through the test strip. If the marker is present in the sample the binding sites on the colloidal gold will become increasingly occupied depending on how much of the marker is present.

Once the binding sites are all occupied or the sample does not contain more of the marker, the sample will collect on the membrane and the intensity of the gold color will depend on how much colloidal gold-labeled antibody was reacted. The intensity of colloidal gold color is the inverse of the concentration of marker present in the sample [2].

Lateral flow test strips can be created to add layers of antibodies for multiple diagnostics. First, there is a pad into which the sample is placed; the sample then flows through the layers interacting with antibodies. If the antigen is present in the sample it will be visually detected. Finally, the sample flows into the absorbent pad. An example lateral flow assay is displayed in Figure 1.

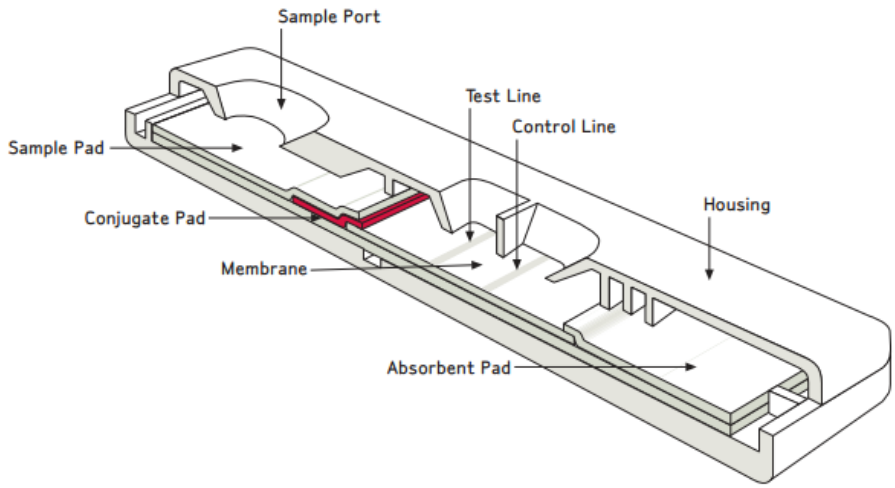

Figure 1: General LFA example that includes the sample port, conjugate pad, and absorbent pad [3].

Simple one dimensional paper-based assays have been extended to three dimensional lateral flow systems that have complex microfluidic paths.

These three dimensional devices have the capability to become low cost analytical systems [4]. The lateral flow systems are small, lightweight, easy to stack, store, and transport, and they do not require external systems to power or pump.

1.2 Colloidal Gold Antibody Conjugation

The use of gold conjugated to antibodies began in 1971 [5]. The uses of colloidal gold conjugates include; as markers for electron microscopy, immunoassay's, microarray's, and light microscopy [5]. Gold markers are useful in lateral flow assays because they have the ability to bind proteins noncovalently. Once bound, the gold will not change the protein's bioactivity [2]. The gold nanoparticles (NPs) are typically conjugated with antibodies that are specific to the molecules of interest. The gold NPs are guided by molecular recognition; they will bind to the antigen or target regions that contain the antigen. Another benefit of gold particles is that they do not suffer from photo bleaching. Therefore, it is not necessary to keep the samples out of the light [6].

When utilizing gold NPs it is useful to optimize antibody-antigen recognition. The Nyocard immunoassay is a technique that utilizes a membrane bound antibody. Detection is possible via an antibody that is conjugated to the colloidal gold. The resultant color signal is proportional to the quantity of sample bound to the membrane antibody. For the success of this technique the antibodies must have high affinity and optimal fastening kinetics.

Various conjugation techniques will affect the binding of antigen with antibody [7]. The goal is to find a high affinity antibody to successfully and sensitively capture antigens from an analyte [7].

Sol (gold) Particle Immunoassay (SPIA) has been utilized with numerous antibodies including, immunoglobin G, immunoglobins from blood of HIV positive patients and cystatin C. BIAcore™ Surface Plasmon Resonance (SPR) is a technology that has the ability to study interacting molecules that are associating and dissociating. Biacore™ SPR can also be used to identify and rank matching monoclonal antibodies. Johne et al. (1995) demonstrated that the BIAcore™ SPR is compatible with gold conjugated proteins. It is able to view the molecular interactions without interference from the gold particles [7].

Conjugating proteins with colloidal gold can lead to diverse affinities for their antigens depending on how the antibodies are immobilized. Safenkova et al. (2010) set out to determine the relationship between the conjugate and its affinity [8]. They used the BIAcore™ SPR biosensor to determine the sensitivity. Colloidal gold particles were used and conjugated to antibodies. They determined that increasing the antibody to NP ratio will produce conjugates that will have higher affinity and therefore will produce superior results when used in bioanalytical situations [8].

1.3 Orange G Dye

Orange G is an acid dye. An acid dye is defined as any brightly colored organic compound that contains both an acid group and produces a color [9]. The molecular weight of the compound is 452.37 g/mole and its color index number is 16230. Orange G is classified under the azo dye class. It absorbs light at 475 nanometers (nm). The color that is observed is the compliment of this light absorption. The visible light spectrum defines 475 nm as blue, its compliment is orange. Its empirical formula is $C_{16}H_{10}N_2O_7S_2Na_2$ [10]. The chemical structure is shown in Figure 2.

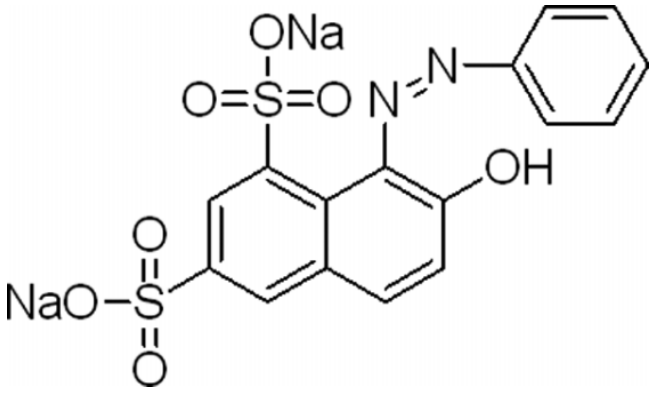

Figure 2: Chemical Compound of Orange G Dye [10]

Orange G dye has a high solubility in aqueous solutions (116 g/L) at 30 degrees Celsius [11]. It has been chosen for use due to its inexpensive cost and accessibility. It also provides a simple model to work with. Orange G dye's visual properties are fairly straightforward whereas, colloidal gold's optical properties are highly dependent on the particles characteristics. The characteristics of colloidal gold will be discussed in the next section.

1.4 Colloidal Gold

Colloidal gold has been used since the 17th century when gold nanoparticles (NPs) were used in dark red stained glass. It was later recognized by Faraday that the pigment was due to the colloidal properties of gold [1]. The light absorption by gold is the clear oscillation of the conduction bands that are created by an interacting electromagnetic field. Plasmon absorption is size dependent, (NP size directly affects the magnitude of the refractive index [12].) The plasmonic properties of the colloidal gold depend on the properties (composition and grain size) of the metallic particles and their concentrations in solution; furthermore, the signaling properties of colloid concentration are also dependent on the properties of the liquid they are suspended in [12].

Colloidal gold is used frequently in scientific applications because of its inert characteristics. To ensure colloidal stability, the particles are commonly enclosed by stabilizing molecules that form a shell. This shell inhibits flocculation and therefore ensures a stable, homogenous suspension. Additionally, colloidal gold is extremely useful because the molecular layer provides an intermediate layer for additional biomolecular functionalization via conjugate chemistry. An example of conjugate chemistries with colloidal gold include the linkage of amino groups with carboxyl groups at the free ends of the stabilizer molecules (antibodies, proteins and nucleic acids) [6].

Gold NPs appear red instead of gold in color due to their surface-plasmon oscillation wave length which peaks at a wavelength of 520 nm, see Figure 3 for the wavelengths of light, by the Mie absorption [13].

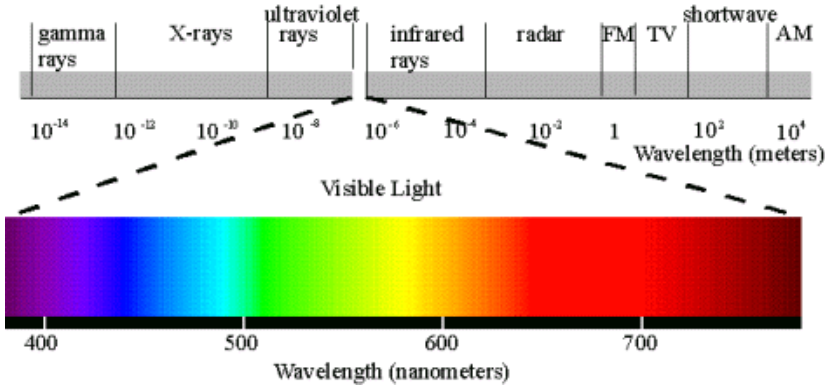

Figure 3: Visible light spectrum [14]

The Mie absorption is better known as the Mie solution to Maxwell's equations. Gustav Mie took the light scattering approximations and the Maxwell equations and produced a theory to describe the optical properties of colloidal gold [15].

Colloidal gold's configuration is confined by its surface plasmon. This allows the particles to produce a unique spectral resonance [15]. Advancements in plasmon resonant particles allowed assays to be developed using gold NPs. The areas that allowed this development were the creation of optical systems to detect the particles, the development of a method to manufacture significant quantities of particles that were congruous, the preparation of nonreactive particles, and the ability to congregate the particles [5].

1.5 Hue, Saturation, and Value

Color can be quantified using many methods. Colors are present or represented in visual experiences. Color spaces specify colors from the three primary colors; red, green, and, blue [16]. There are many color spaces to quantify color and they can be classified into four groups that are connected by different types of transformations; linear light tristimulus, this color space was created by the International Commission on Illumination (CIE) (CIE XYZ, and CIE RGB), xy chromaticity (CIE xyY), perceptually uniform, and hue oriented (HLS, HSV)[16]. The red, green, blue (RGB) color space is used by scanners and digital cameras; it is an additive representation as all of the colors can be represented as a combination of red, green and blue when these three colors are combined [17]. The hue, saturation, value (HSV) color space is derived from the red, green, and blue intensity values, but a pixel in this color space is defined by its hue, saturation, and value coordinates. RGB is not as intuitive for the mind to understand as HSV is, mainly due to its Cartesian coordinates. Hue is a numerical representation of color; any specific color is a hue. Saturation determines the degree to which a single channel dominates; it is the purity or shade of a color. Value represents color brightness or lightness.

Equations 1-3 display the necessary calculations in order to convert from RGB to HSV [16].

$$H = \cos^{-1}\left\{\frac{\frac{1}{2}[(R-G)+(R-B)]}{\sqrt{(R-G)^2+(R-B)(G-B)}}\right\} \quad (1)$$

$$\boldsymbol{S = 1 - \frac{3}{R+G+B}[\min(R, G, B)]} \quad (2)$$

$$V = \frac{1}{3}(R + G + B) \quad (3)$$

Here R, G, and B are the red, green, and blue color intensities, respectively and min is the minimum values of R, G, and B. Hue is dependent on wavelength of light, but also varies in response to the Bezold-Brucke effect and the Abney effect. The Bezold-Brucke effect is the concept that changing the brightness or intensity of light will affect the hue. As brightness increases reds and yellows will become more orange and yellow [18]. The Abney effect is the notion that as white light is added (desaturation) hue will change; blue will appear more purple and orange will appear more red [18].

The main difference between the HSV and RGB color space is that HSV takes into account intensity of the image whereas, RGB does not. HSV is derived from RGB in the sense it uses the intensity of the red, green, and blue color values [19].

The three dimensional representation of HSV is a hexacone (Figure 4).

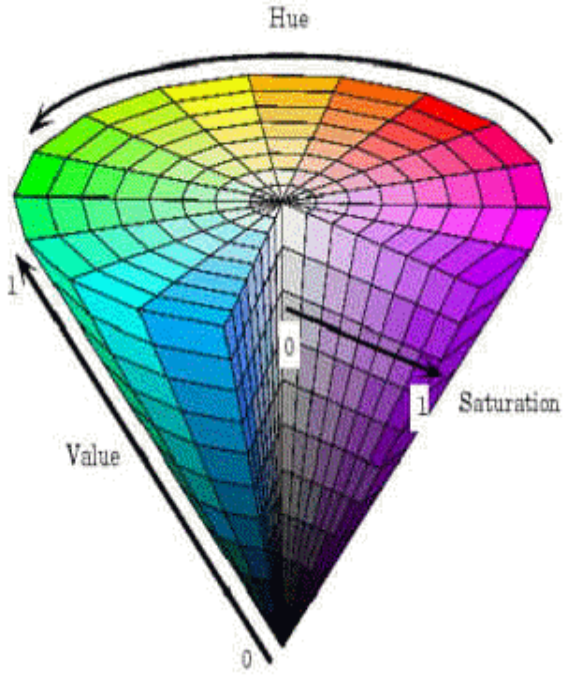

Figure 4: The HSV hexacone [20]

Value is the central vertical axis, hue is an angle that can range from zero to 2π, and lastly, saturation is the purity of the color, measured from zero to one from the central axis at zero to the outer surface at one. The HSV hexacone representation is straightforward to understand; the hue is the color, saturation is the shade of that color, and value is essentially the grey scale of color.

The value axis moves from black to white and gets there via various shades of grey. If saturation is decreased while hue and value remain fixed the resultant color will be a shade of grey. The shade of grey is dependent upon value. If saturation is at or near zero all of the pixels will appear the same, but as it is at or near one the pixels are separate and can be perceived as color.

Therefore, if an image has a low saturation value the grey value will produce the color whereas, if it has a high value, hue will produce the color. Depth of color is determined by saturation [19]. HSV values are stable, easy to calculate, are easily obtained from image analysis software, and their values are analyzed between zero and one therefore, this is a prime color space for image analysis.

Digital images are comprised of pixels, which are elements of images. A pixel is the smallest element of an image and each pixel can only be associated with one color (iPhone5 has a pixel per inch value of 326) [21]. In order for the image to be analyzed, the pixels must be categorized. This can be done using a histogram. A histogram graphically represents the color of an image. Histograms can be generated using the HSV color space. The pixels are analyzed and categorized. Each image's color can be broken down into bins. The amounts of bins are determined by the possible color values that an image class can have.

1.6 Technology and Unaided Human Eye Capabilities

Light has both wave and quantum properties. Photons are quanta of light energy. Photons have a fixed amount of energy. This energy can be calculated by equation 4:

$$E = hf = \frac{hc}{\lambda} \qquad (4)$$

Where h is plank's constant, 6.63×10^{-27}, f is the frequency, c is the speed of light, and λ is wavelength in nm.

The structure of the human eye can be viewed in Figure 5A, along with a magnification of the eye's light sensor Figure 5B. Light enters the eye via the cornea and is focused by the lens [22].

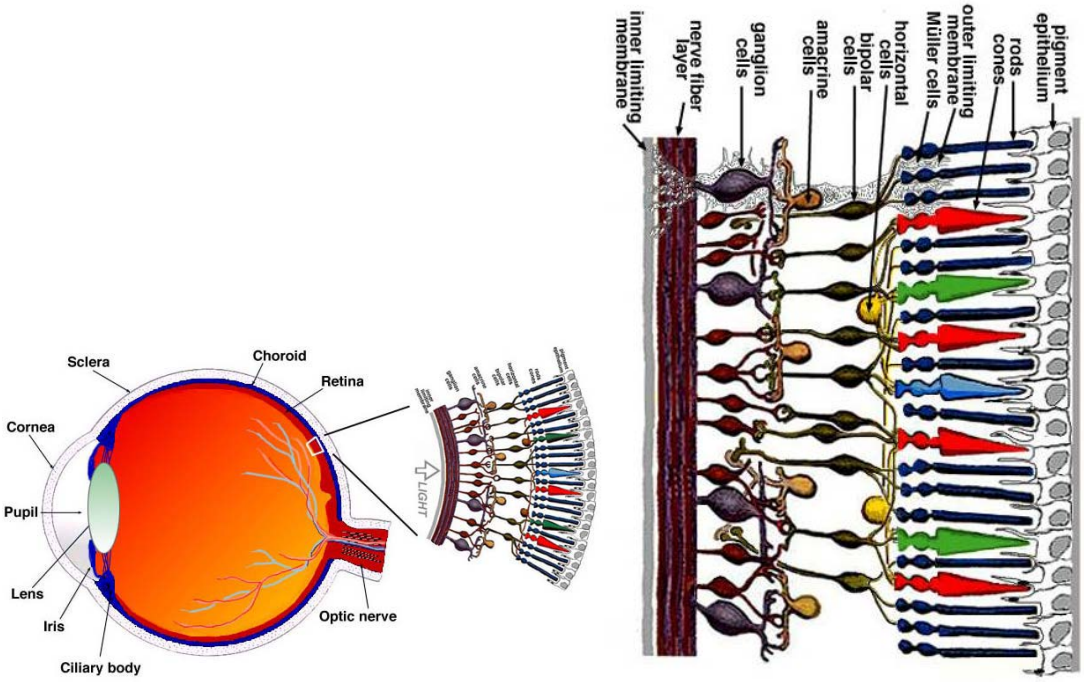

Figure 5: A. Human eye structure B. Magnification of light sensor [22]

The eye's light sensor is a layered structure about 0.5 millimeters (mm) thick. This sensor covers about 70 percent of the surface of the eyeball. As shown in Figure 6, the human eye has two types of photoreceptors; rods and cones.

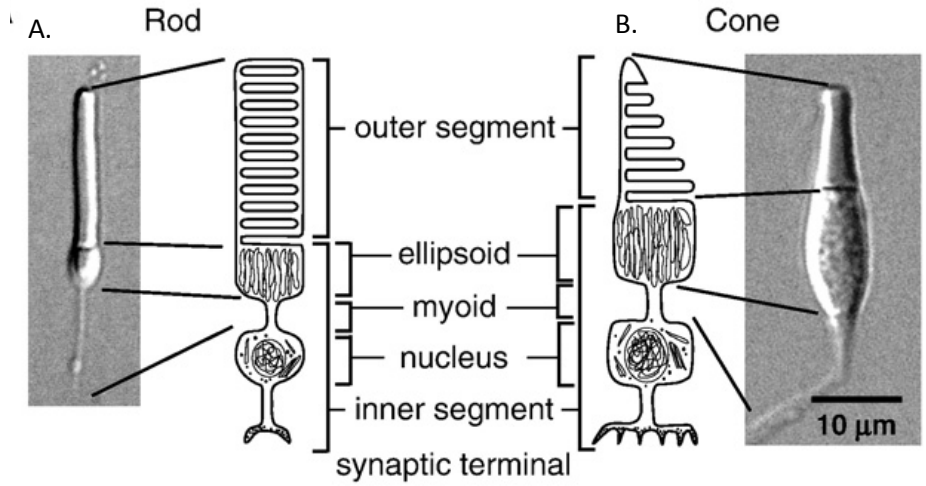

Figure 6: A. Diagram of a rod B. Diagram of a cone [23]

These photoreceptors have an inner and outer segment. The outer segment of the photoreceptors is the portion of the retina that detects a photons signal. There are approximately 6-7 million cones in the eye, which are sensitive to color, but not sensitive to light intensity therefore, they deliver precise color vision in bright light. There are approximately 75-150 million rods in the eye. They are sensitive to light intensity and motion, but not to color therefore; they provide vision in dim light. Rods are most sensitive to wavelengths of light in the range of 500-640 nm. This phenomenon is known as the Purkinje effect [22].

The human eye is sensitive to a minimum of about five photons. Each rod is sensitive to one photon and rods are excited by a photon when it induces an electrochemical reaction. Optimally, the human eye can resolve an image if the angle between two points is equal to or greater than the critical value.

This critical value is calculated using equation 5:

$$\theta = \frac{1.22\lambda}{d} \quad (5)$$

Here λ is the wavelength of light and d is the diameter of the aperture.

The smallest detail an unaided eye can observe is calculated using equation 6 and equation 7 (if θ is very small):

$$\tan^{-1}\frac{\theta}{2} = \frac{h/2}{20} \quad (6)$$

$$\theta = \frac{h}{20} \quad (7)$$

Where h is the height of the object. This smallest detail is calculated to be 0.1 mm for the optimal case presented in Figure 7 [22].

Figure 7: Diagram of unaided eye resolving power [22]

Each person has a different resolving power depending on imperfections of their lens system and in the structure of their retina. Consequently, the benefit of using an image taken from a camera or smart phone is that the image will always be the same under the same conditions. Each camera in a specific type of device should behave in the same manner with the same properties [24].

The human eye can be compared to a camera or in the context of this study a smart phone, as the camera was originally designed to mimic the eye.

Table 1 presents this comparison, “image” quality of the eye will improve with a smaller iris aperture size, because as aperture size decreases it uses the optimal part of the lens and increases the depth of field [22].

Human Eye	Iphone 5 Camera
Iris (2-8mm, dependant on intensity of light)	Aperture (f/2.4)
Cornea and Lens	Lens
Retina	CCD (digital images,film)

Table 1: Human eye to Iphone5 comparison

1.7 Smarphone/MatLab® Imaging

Mobile phone technology has exponentially increased over the years and with that increase mobile phone imaging capabilities and processing powers have continually improved; furthermore, applications are now available to be utilized with many smart phones. As a consequence, the market for smart phones associated with these applications has steadily grown [25]. With the combination of a mobile phone, an advanced optical digital camera, multi-processor computing power and all of the functions of a Personal Data Assistant (PDA), smart phone technology has been embraced not only for personal use but for clinical and scientific as well. This is due to the ability of the user to easily and compactly collect, transmit, and organize data [25]. Here lies the parallel between smart phones and LFIA.

Many integrated methods have been proposed for combining paper-based microfluidic devices that use channels of hydrophilic paper lined with a hydrophobic polymer and imaging devices that are capable of obtaining colorimetric results, quantifying the results, and transmitting the results [26]. The use of technology and mobile devices to improve the accessibility and quality of health care are referred to as electronic and mobile health [25].

1.8 Nitrocellulose membrane

Most commercial lateral flow assays utilize a Nitrocellulose membrane for the detection region of the device, see Figure 1 above; therefore the detection membrane is an extremely important element to consider when designing a lateral flow assay. Polymer selection must optimize binding for all molecules of interest. A polymer's available surface area determines this faculty. This surface area is characterized by pore size, thickness, porosity, and any polymer specific structural characteristics [3].

Nitrocellulose membrane paper uses electrostatic interactions to bind particles [3]. The particles are bound by a strong dipole. When interacting with proteins the strong dipole of the nitrate ester interacts with that of the proteins peptide bonds.

Figure 8 shows the configuration of the nitrate and peptide bonds.

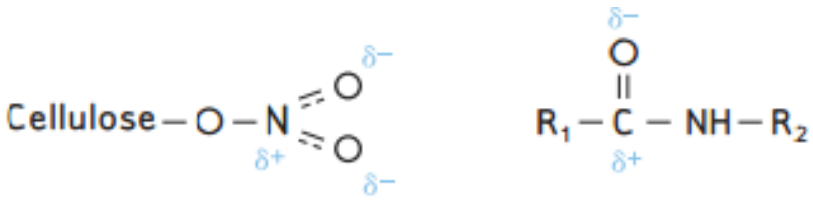

Figure 8: Nitrocellulose ester and protein dipole structures [3].

Capillary flow rate is also an important characteristic to consider when addressing membrane. Capillary flow time is used to determine the flow rate, as they are inversely related. Flow rate is extremely difficult to measure due to an exponential decay rate. Table 2 displays the capillary flow times of various membranes.

Membrane	Capillary Flow Time Specification* (sec/4 cm)	Flow Rate	Sensitivity
HF240	240 ± 60	Slowest	Most sensitive
HF180	180 ± 45		
HF135	135 ± 34		
HF120	120 ± 30		
HF090	90 ± 23		
HF075	75 ± 19	Fastest	Least sensitive

*The range is for all measured values on a roll and represents ± 3 ∂; the acceptable range for the mean is ± 10% of the target.

Table 2: Capillary flow times [3].

Another important variable to take into account is to visually analyze the membrane. Therefore, the percent of the perceptible signal is important to be aware of. It is related to the membrane thickness by equation 8.

$$\%\, Visible\ Signal = \frac{Visible\ Depth\ (\sim 10\ \mu m)}{Membrane\ Thickness} \qquad (8)$$

Backed nitrocellulose membranes are easier to handle and print on.

Nitrocellulose paper has the feature of the ability to be patterned into channels. The hydrophilic paper is separated by the hydrophobic walls [3]. These walls in the paper direct the fluid into detection zones so that assays may take place.

1.9 Current cell phone technology

Currently there is smart phone technology that utilizes an attachment that is placed on the phone. This attachment is designed and printed so that a lateral flow device can be inserted. Once inserted the device utilizes Mie scatter to optimize the visual parameters [27]. Another group Wang et al. (2009) have used smart phones with microfluidic technology for tuberculosis (TB) diagnosis [2]. A cell phone is used for fluorescence microscopy; however this approach necessitates the use of expensive lenses and filters. The imaging system itself is quite complex. Breslauer et al. (2009) have also developed a high resolution microscope attachment for smart phones [28]. This technology enables clinicians or even civilians in remote areas to image samples that can be used for TB and malaria diagnosis.

The design of this complex microscope may be viewed in Figure 9.

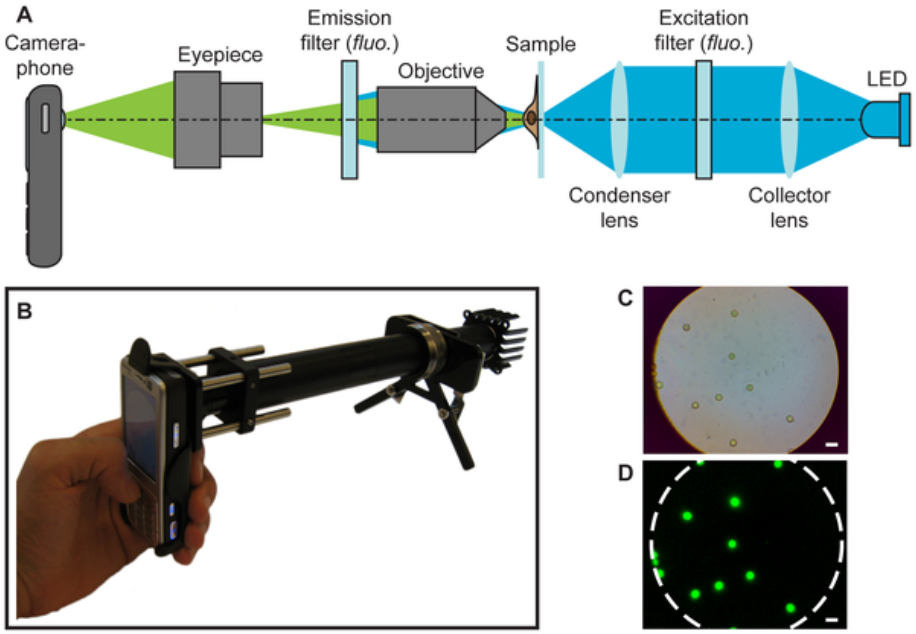

Figure 9: Smart phone microscope adaption [28].

This allows a smart phone to become a microscope. The images can then be sent to a lab to be analyzed [28].

1.10 Objective

A low cost compact diagnostic has many indications in today's society. There are many regions within the United States and in developing countries in which the large diagnostic devices are unavailable. Individuals who require this bulky expensive equipment must travel extensive distances to a hospital or medical center that is equipped with the necessary tools. In many cases this journey is too cumbersome or unavailable. Another indication where this would be useful is within NASA, while astronauts are in space they are required to take daily blood and urine samples.

These samples are then stored on the spacecraft. By doing so a vast amount of space is essentially wasted housing these samples. In both cases the availability of a low cost compact diagnostic would be extremely beneficial.

Smart phone technology has exponentially grown and with it the imaging capabilities of these smart phones. The goal of this study is to use an image taken with a smart phone as a diagnostic. A lateral flow assay will be created and once the sample has been processed an image of the results will be taken with the smart phone. The same luminosity should be used for image capture. The image will then be uploaded into a developed MatLab® image analysis code, utilizing the HSV color space; the analysis will break down the pixels and bins to classify the result depending on calibration equations obtained from the specific smart phone device.

The goals of this research are i) to determine the feasibility of combining in the field smart phone images with color dependent assay results, ii) to develop a MatLab® image analysis code to analyze these results, and iii) compare limits of detection between the un-aided eye and MatLab® image analysis software. The results from this study can be used to further develop an LFA or LFIA that can be used in combination with the developed image analysis code.

2. METHODS

2.1 Sample Preparation

In high concentrations colloidal gold is expensive as are antibodies that could be conjugated to the gold NPs, therefore as a proof of concept Orange G dye is used. A stock solution was prepared using 0.02 grams (g) of Orange G dye (obtained from Sigma Life Science) and 100 milliliters (ml) of distilled (DI) water. The dye was weighed using an Acculab Scale. The stock solution was then diluted with DI water according to the experiment. Equations 9 and 10 were used to solve for concentration.

$$Concentration\ (C) = \frac{mass(m)}{Volume(V)} \quad (9)$$

$$C_1V_1 = C_2V_2 \quad (10)$$

2.2 Nitrocellulose membrane preparation

Sheets of backed nitrocellulose paper were obtained from Millipore. AutoCad was used to design an assay platform of circular wells. Well diameter was determined by analyzing six well diameters, ranging from 2-9 millimeters (mm), the optimal well diameter was found to be 7 mm. Next 10x10 circular wells were printed on the nitrocellulose paper using wax ink. They were printed using a Color Qube 8570 wax printer from Xerox ®. According to Lu et al. (2008) (26), the printed wells were heated on a hot plate (IKAC-Mag HP 10) for 5 minutes at 125 degrees Celsius.

Well volume was calculated by equation 11 and found to be 2.969 microliters (µl).

$$V = \pi r^2 h \qquad (11)$$

Where V is volume, r is radius and h is well height. The well diameter after heating was 6mm. Figure 10 displays the 10x10 circular wells after baking.

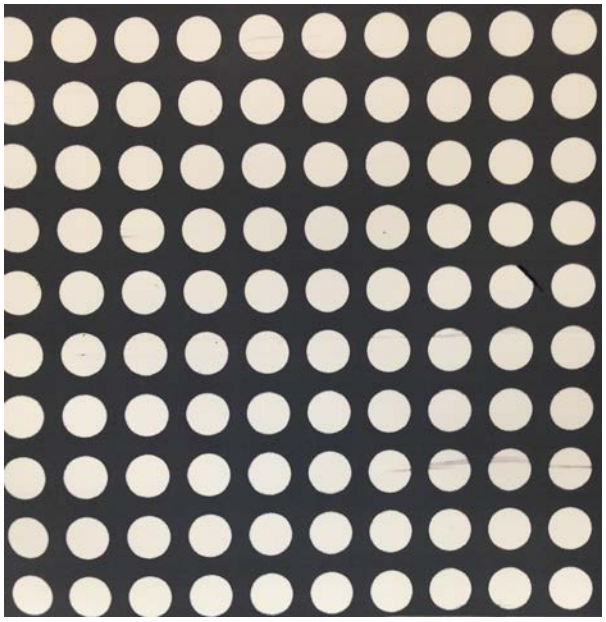

Figure 10: Assay platform of 10x10 baked circular wells designed in AutoCad

2.3 MatLab® Image Analysis Code

With the help of Nora Candido and Natasha Johnson a MatLab® image analysis code was developed. This code utilizes the HSV color space to analyze the pixels of images. The HSV color space is more intuitive then the RGB color space and as shown in equations 1-3 hue, saturation and value are each calculated by using an intricate combination of RGB values. Initially, hue, saturation, and value are outputted from the analysis; these values are then used to modify the code to obtain concentration. Figure 11 details highlighted portions of the image analysis code.

Part A is the while loop and the device selection option, the code loops so that analysis can continue until terminated. Part B allows for the sample image to be opened and cropped. Part C outputs the values of RGB and part D converts the image from RGB to HSV color space. Part E separates and plots the image into hue, saturation, and value layers for analysis. Part F calculates the values for average hue, saturation, and value, these values will be used to form calibration equations to obtain the approximate concentration which is completed in part G. Lastly, part H is the end of the while loop where the user is able to carry out further analyses or terminate. The complete code is provided in appendix A.

```
while(1)

intake=input('Select Device Used 0=iphone5, 1=scanner, 2=iphone4, 3=iphone3Gs:');

buffer=pwd; %load file
[file, pathname] = uigetfile('*.jpg','Load Image');
cd(pathname);
color_image1=imread(file);
cd(buffer);
a=size(color_image1,3);

    figure(1) %crop file
    color_image2=imcrop(color_image1);
    imshow(color_image2);
    save color_image2;

RGB =mean(color_image2);
R = mean(RGB(:, :, 1));
G = mean(RGB(:, :, 2));
B = mean(RGB(:, :, 3));

hsv_image = rgb2hsv(color_image2); %conversion from RGB to HSV

image_h = hsv_image(:,:,1); %HSV layer separation
image_s = hsv_image(:,:,2);
image_v = hsv_image(:,:,3);

    figure(2)
    subplot(3,3,1), imshow(image_h), title('Hue Image');
    subplot(3,3,2), imshow(image_s), title('Saturation Image');
    subplot(3,3,3), imshow(image_v), title('Value Image');

    subplot(3,3,4), imhist(image_h);
    subplot(3,3,5), imhist(image_s);
```

A. Beginning of while loop and option to select the device used

B. Allows image to be opened for analysis

C. Analyzes the image for the average values of red, green, and blue pixels

D. Converts from RGB to HSV color space

E. Plots separate histograms for hue, saturation, and value

```
    subplot(3,3,6), imhist(image_v);

%Uses any nonzero Counts and Calculates Average
    [rowHCounts]=find(hueCounts);
    ValuesofHueCount=hueCounts(rowHCounts,1);
    ValuesofHueBin=hueBinValues(rowHCounts,1);
    AverageHue=mean(ValuesofHueBin)

    [rowSCounts]=find(saturationCounts);
    ValuesofSaturationCount=saturationCounts(rowSCounts,1);
    ValuesofSaturationBin=saturationBinValues(rowSCounts,1);
    AverageSaturation=mean(ValuesofSaturationBin)

    [rowVCounts]=find(valueCounts);
    ValuesofValueCount=valueCounts(rowVCounts,1);
    ValuesofValueBin=valueBinValues(rowVCounts,1);
    AverageValue=mean(ValuesofValueBin)
```

F. Calculates the average values of hue, saturation, and value using bins

```
%Best Fit Equations Separated by "intake" selection
if intake == 0

       Approximate_Concentration=-0.0658*(AverageHue^2)-0.0219*(AverageHue)+0.0043

       Approximate_Concentration=0.0015*log(AverageSaturation)+0.0036

       Approximate_Concentration=-0.2005*(AverageHue^2)+.0045*(AverageHue)+0.003

       Approximate_Concentration=-0.0072*(AverageSaturation^2)+0.0096*(AverageSaturation)-
0.0004
```

G. Calibration equations used to calculate the concentration from mean hue and saturation values

```
choice = menu('Press yes no','Yes','No');
if choice==2 | choice==0
   break;
```

H. End of while loop, gives a choice to run another analysis or stop

Figure 11: Portions of image analysis code. A. While loop of the code and device selection B. Image upload C. RGB output D. Converts RBG to HSV color space E. Plots the histograms of hue, saturation, and value F. Calculates the average values of hue, saturation, and value G. Calculates approximate concentration H. End of while loop.

Starting the code produces a prompt for the type of device used as seen in Figure 12. The code has the ability to use multiple calibrations from different devices and the analysis will depend on which device was selected.

Select Device Used 0=iphone5, 1=scanner, 2=iphone4, 3=iphone3Gs:

Figure 12: Image analysis code prompt to select device used

0 is entered for Iphone5, then the image is selected, as displayed in Figure 13.

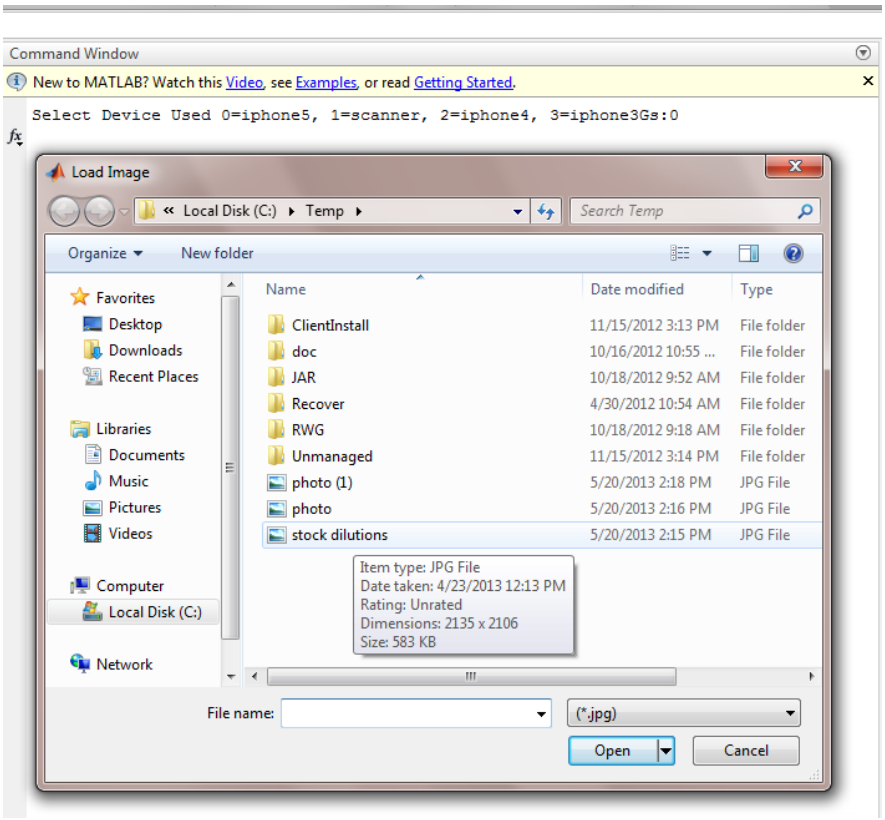

Figure 13: Screen shot of image load screen.

Using the select tool, one of the wells was selected and then, displayed in Figure 14A, using the zoom button the image was zoomed in twice.

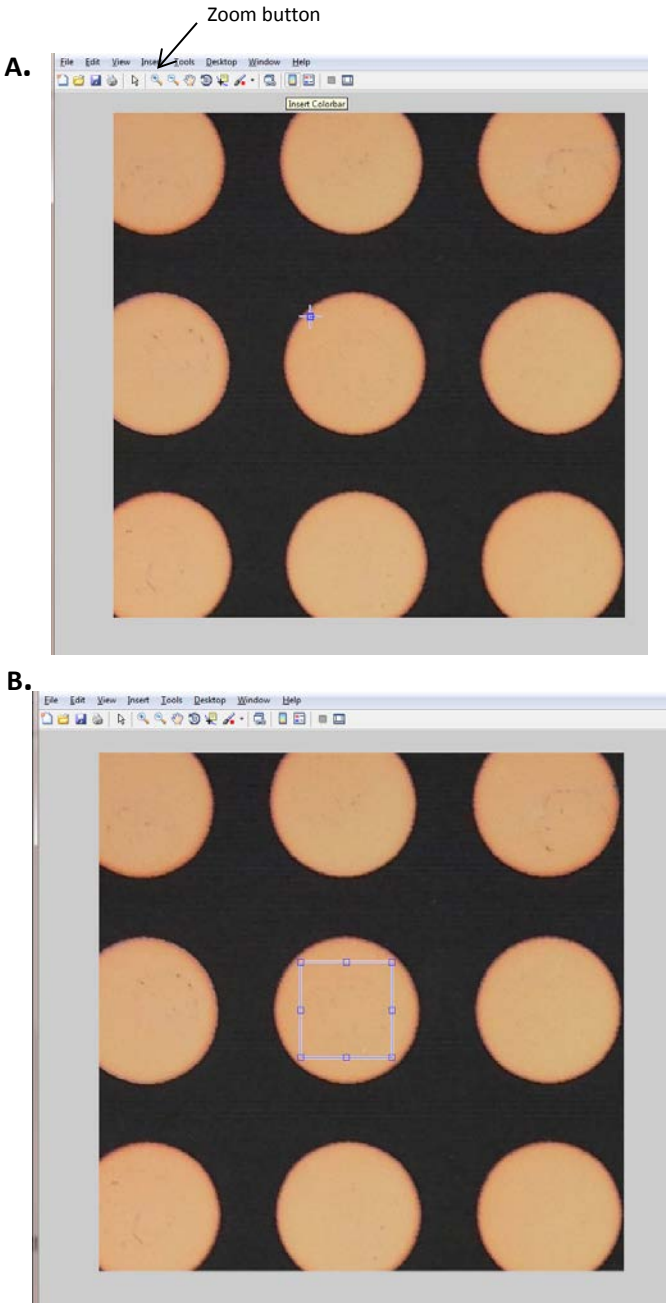

Figure 14: A. displays the zoomed in well. B. displays the box made around the well that was subsequently selected.

Then, a box was made over one of the wells selecting it (Figure 14B). Once selected, the code runs and outputs the values of average hue, saturation, and value, the code also provides a histogram and the cropped image as seen in Figure 15.

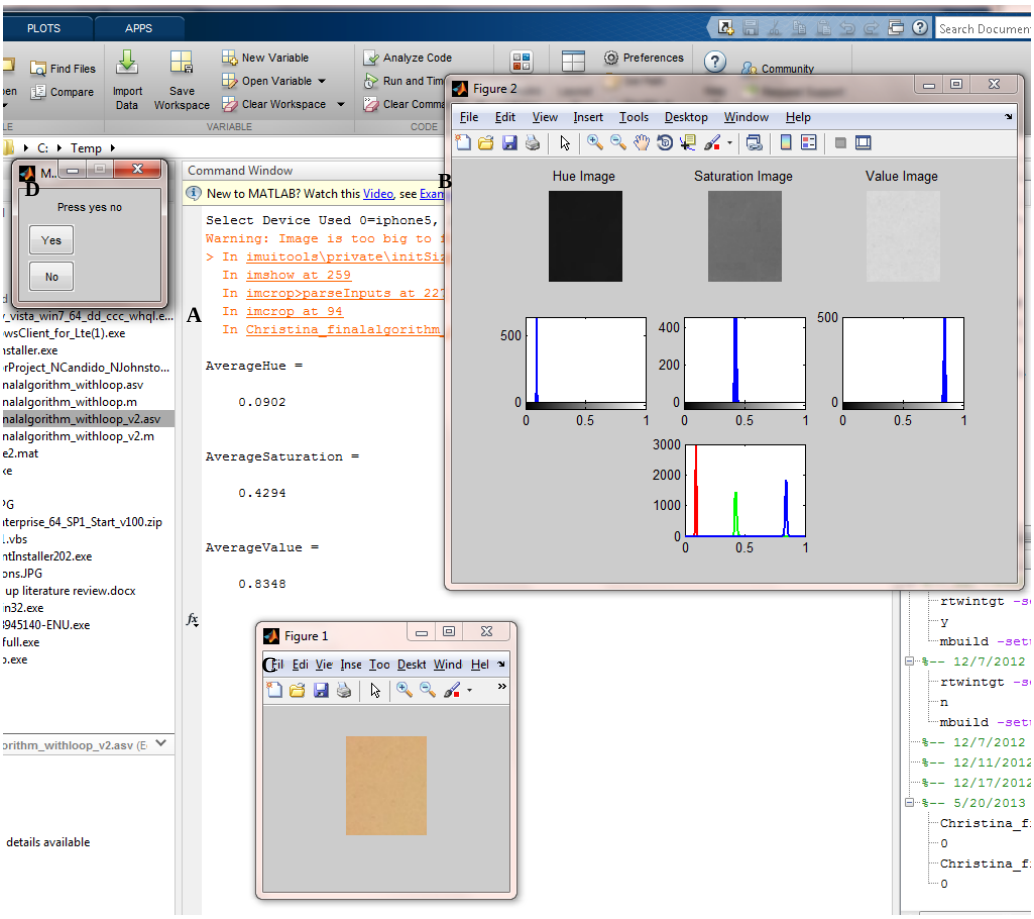

Figure 15: Screen shot of image analysis code outputs. A. Values of average hue, saturation, and value B. Histograms of hue, saturation, and value C. Area selected from well sheet image D. choice to continue with another analysis or end by clicking no.

2.4 ImageJ Cross Check

It was necessary to cross check the validity of MatLab® to produce HSV values for HSV. ImageJ was used for this purpose. ImageJ is the standard for image analysis. Red, green, and blue values were obtained from MatLab® and then from ImageJ. These values were averaged for the treatment levels and plotted.

2.5 Limit of Detection

A limit of detection study was necessary in order to collect a yes, no, or maybe answer from a lateral flow assay. For example, perhaps it is necessary to test for salmonella, the main concern is whether the marker is present or not.

For this procedure limit of detection was determined by analyzing the nitrocellulose paper with no sample. Next samples of various concentrations were analyzed ranging from $2.00e^{-5}$ to $1.18e^{-4}$ mg/ml. Figure 16A provides a sample of the wells from the limit of detection experiment and Figure 16B provides the target concentration values.

A.

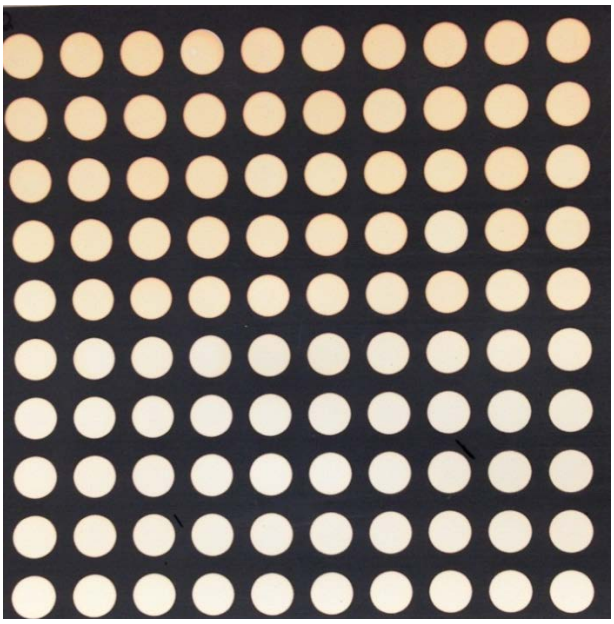

B.

.001
.0009
.0008
.0007
.0006
.0004
.0002
.000196
.000192
.000187

Figure 16: A. Limit of detection well dilutions B. Concentration values of each row in g/ml.

2.6 Calibration of MatLab® Image Analysis Code

In order to apply the MatLab® image analysis code to determine concentration it must first be calibrated. A 10x10 sheet of wells was used for the calibration. Nine dilutions were performed beginning at a stock solution concentration of 0.002 g/ml the dilutions decreased the concentration by 0.0001. Once the dilutions were performed 2.969 µl were pipetted into each well. Each row contains the same concentration or treatment. The sheet was left to dry for ten minutes and then the sheet was imaged with an Iphone 5 camera (8 megapixel f(2.4 aperture) [21]. The image was taken six inches away from the sample sheet. The sample and smart phone were placed parallel to each other and laboratory ambient lighting was used for the imaging. Figure 17A is the imaged calibration wells and 17B is the concentration values of each row of wells.

A.

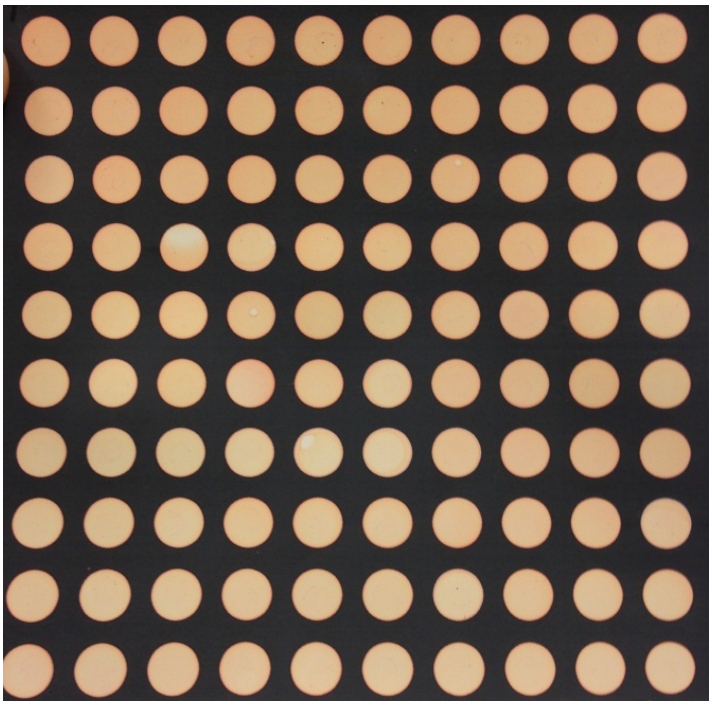

B.

.002
.0019
.0018
.0017
.0016
.0015
.0014
.0013
.0012
.0011

Figure 17: A. Calibration wells. The wells begin at a concentration of 0.002 g/ml and finish at a concentration of 0.0011 g/ml B. Concentration values of each row in g/ml.

In order to perform the calibration the average hue, saturation, and value output values were unhidden in the image analysis code. The MatLab® code was then run. This process was repeated for each well of the 10x10 sheet. Once all of the values were obtained in Excel the ten values of each concentration were averaged and a trimmed mean of five percent was also calculated to eliminate outliers. The values were then plotted for hue, saturation, and value to determine if a relationship existed between the concentration and hue, saturation, and/or value.

2.7 Experimental Analysis

After creating the calibration wells another sheet was made to perform various dilutions using the same protocol that was used for the calibration. Please see Figure 18A and B. These experimental wells were analyzed via the image analysis code. The MatLab® code was run using the new well sheet, which produced concentration values based upon the calibration equations obtained.

A.

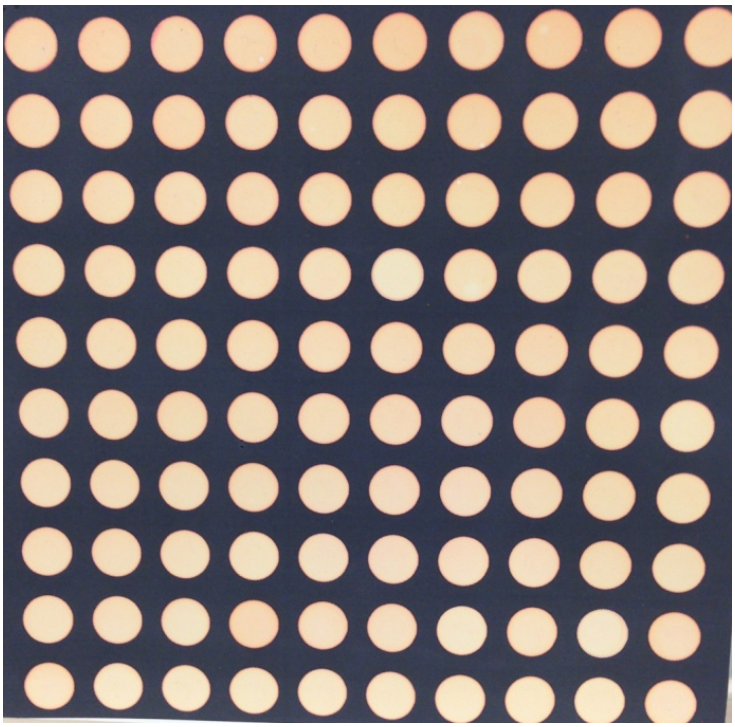

B.

.002
.001818
.00167
.00154
.00143
.00133
.00125
.001176
.00111
.00105

Figure 18:A. Experimental well dilutions B. Concentration values of each row in g/ml.

2.8 Spot Check of Experimental Analysis

A spot check was then performed to test whether the data was consistent. A sheet of 10x5 wells was created and imaged according to the calibration protocol to compare with the experimental analysis. A separate stock solution was made with a concentration of 0.02 g/ml and dilutions were made from the stock solution. Figure 19 A and B display the spot check wells.

A.

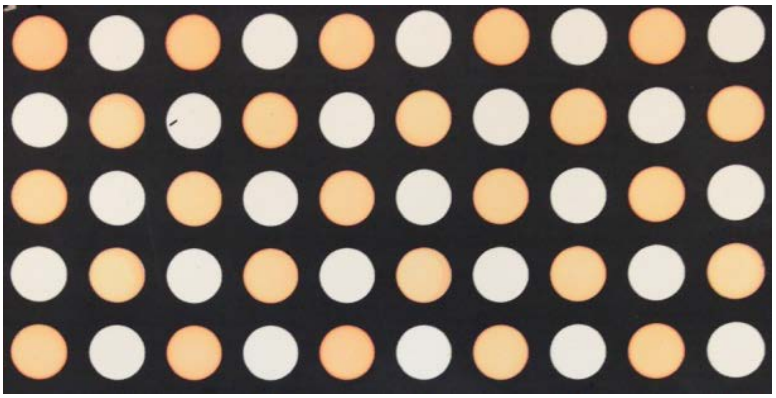

B.

.002
.00167
.00154
.00143
.00133

Figure 19: A. Spot check well dilutions B. Concentration values of each row in g/ml.

2.9 Error Analysis

There was an assortment of errors associated with the stock solution formation. The scale used for weighing the dye is old and contains residue therefore, the error of the scale was taken to be ±0.0025g. A 100 ml graduated cylinder was used to measure the DI water and therefore, the error of this measurement is ±0.5 ml. When performing dilutions of the calibration, experimental, and spot check an extra ±0.05 ml error was taken into account.

For the limit of detection experiment as more DI water was needed the error increased accordingly. Another avenue of error is seen in figure 10; where wax printing often produced inconsistencies on the nitrocellulose paper.

Absolute error of the concentration was calculated using equations 12-15. An example calculation was performed.

$$Mass\ Concentration\ \rho = \frac{m}{V} \quad (12)$$

$$\frac{\partial \rho}{\partial m} = \frac{1}{V} \quad (13)$$

$$\frac{\partial \rho}{\partial V} = \frac{m}{V^2} \quad (14)$$

$$\delta\rho = \left|\frac{\partial \rho}{\partial m}\right| \delta m + \left|\frac{\partial \rho}{\partial V}\right| \delta V \quad (15)$$

Where $\delta m\ is\ 0.0025g$, $\delta V\ is\ 0.5ml$, m is mass, V is volume, and $\delta\rho$ is absolute error.

Example Calculation

$$absolute\ error = \delta\rho = \frac{1}{100ml}(0.0025g) + \frac{0.2\ g}{100ml^2}(0.5ml) = \pm 0.00021 g/ml$$

3. RESULTS

3.1 ImageJ Cross Check

From the red, green, and blue values obtained from MatLab® and ImageJ plots were formed comparing the average red, green, and blue values obtained from both programs. These plots are displayed in Figure 20. The percent differences between the RGB values obtained from MatLab® and ImageJ are presented in Table 3.

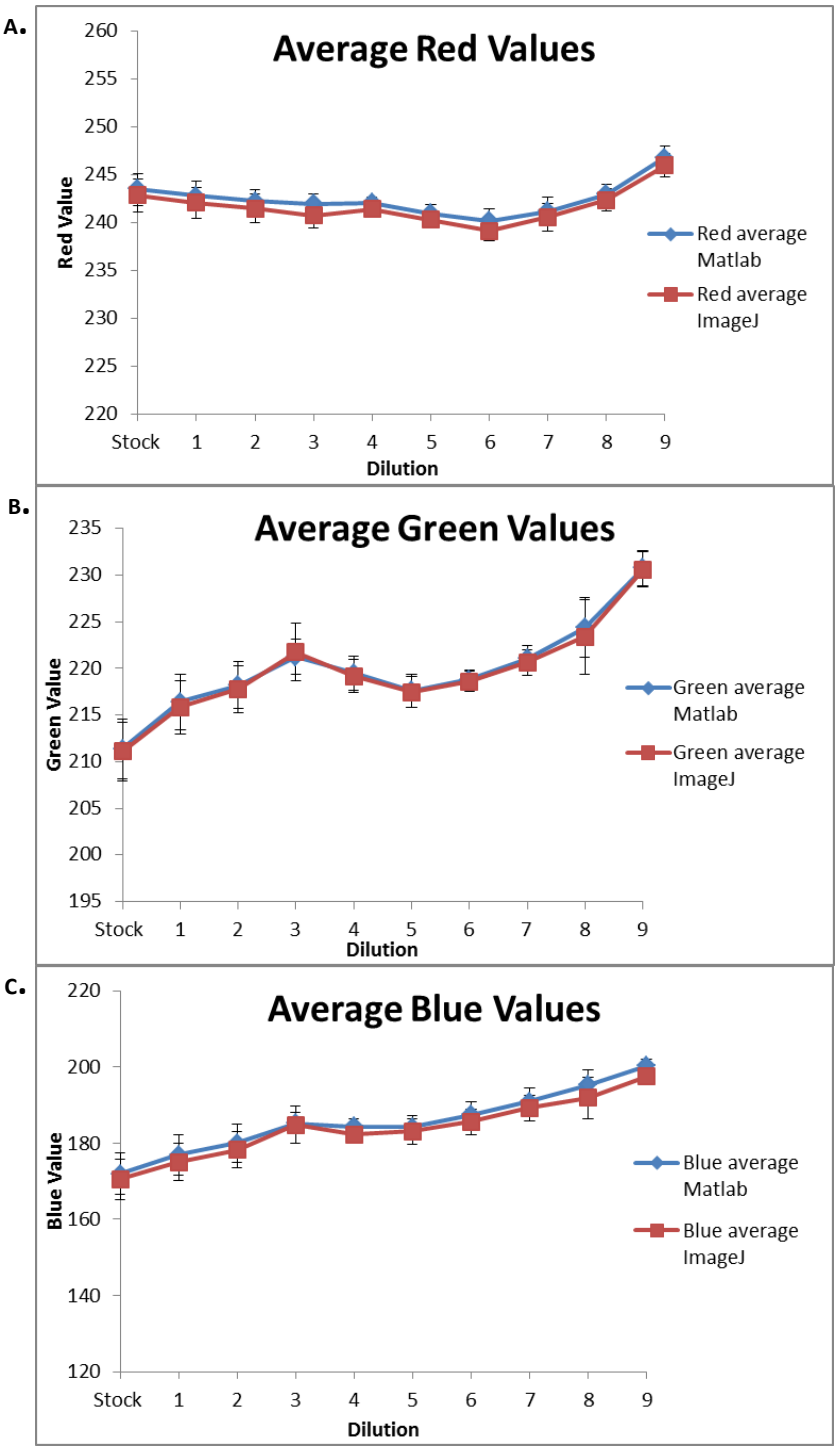

Figure 20: Plots comparing average RGB values obtained from MatLab® and ImageJ

Concentration (g/ml)	Red %	Green%	Blue%
0.002	0.286	0.143	0.848
0.001818	0.294	0.267	1.09
0.00167	0.308	0.193	0.991
0.00154	0.528	0.235	0.245
0.00143	0.279	0.158	1.13
0.00133	0.285	0.069	0.653
0.00125	0.438	0.099	0.955
0.001176	0.258	0.195	0.862
0.00111	0.242	0.448	1.72
0.00105	0.338	0.064	1.47

Table 3: RGB percent difference between MatLab® and ImageJ outputs

3.2 Limit of Detection

The limit of detection experiment resulted in the data in Table 4 and another table that summarizes the average HSV values is available in Appendix B. Table 4 compares the HSV values to the baseline of a concentration of 0 g/ml and results in a percent difference.

Concentration (g/ml)	% Difference Mean Hue	% Difference Mean Saturation	% Difference Mean Value
1.18e-4	10.2	34.4	3.00
1.00e-4	1.30	87.2	-0.040
8.00e-5	5.22	62.9	-.327
5.71e-5	6.12	29.8	.418
5.00e-5	11.0	6.97	.827
4.00e-5	4.68	51.3	-4.30
3.33e-5	6.56	32.6	-3.15
2.86e-5	14.4	9.88	-1.76
2.50e-5	14.3	-9.32	-2.20
2.22e-5	16.1	-22.5	-5.22
2.00e-5	18.3	-6.81	-3.90

Table 4: Percent difference between HSV of sample and baseline.

3.3 Calibration of MatLab® Image Analysis Code

The MatLab® code outputted HSV values for each well. These averaged and trimmed mean values were plotted and are shown in Figure 21. The data obtained from value was scattered, but the data from hue and saturation appear to trend.

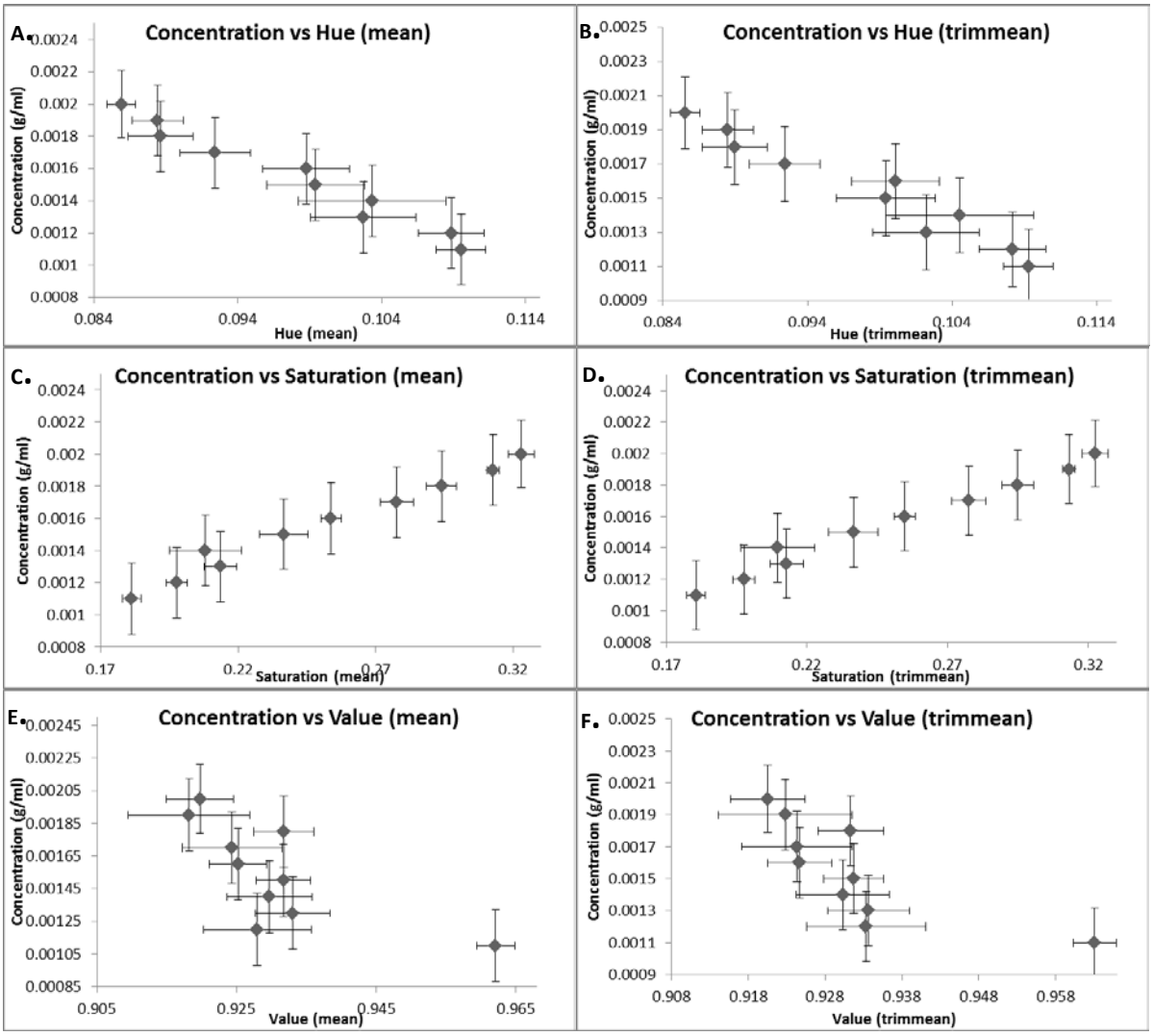

Figure 21: Plots of Concentration vs. HSV. A. concentration vs. mean hue B. concentration vs. trimmed mean hue C. concentration vs. mean saturation D. concentration vs. trimmed mean saturation E. concentration vs. mean value F. concentration vs. trimmed mean value.

These trends are visible in Figure 21 A-D. Next, curve fits were plotted for all six graphs (Figure 22). The curve fits were plotted to optimize the R^2 value.

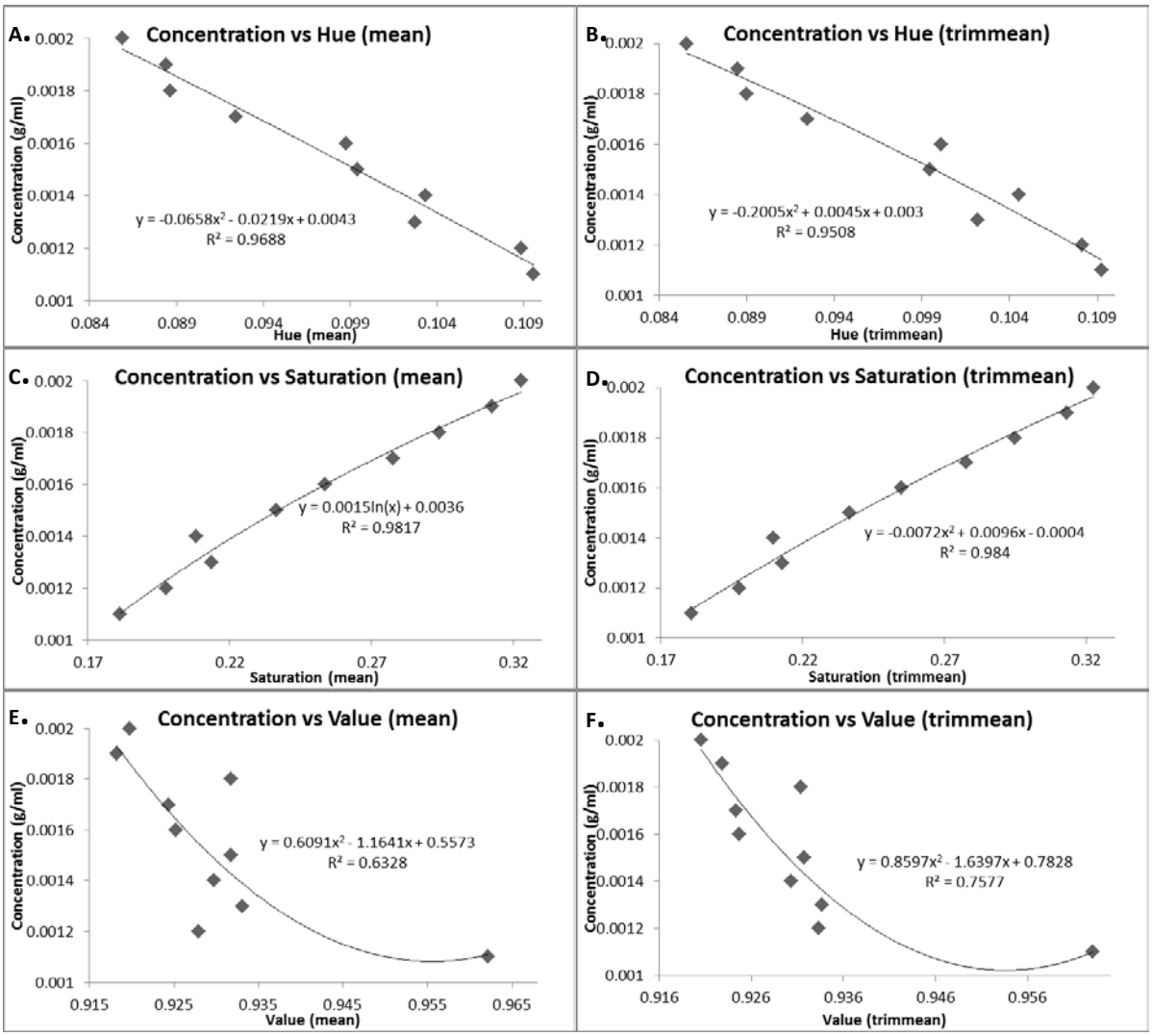

Figure 22: Trend lines of concentration vs. HSV plots. A. concentration vs. mean hue B. concentration vs. trimmed mean hue C. concentration vs. mean saturation D. concentration vs. trimmed mean saturation E. concentration vs. mean value F. concentration vs. trimmed mean value.

The R^2 values for hue and saturation were all above 95%. The value R^2 value was drastically lower, therefore the equations obtained from hue and saturation were input into the image analysis code to solve for concentration. Due to the R^2 values in Figure 22 A-D being relatively high and close all four equations were used in the code to see which produced superior concentration results. Please see equations 16-21 below.

$$y = -0.0658x^2 - 0.0219x + 0.0043 \quad (16)$$

$$y = -0.2005x^2 + 0.0045x + 0.003 \quad (17)$$

Where y is approximate concentration and x is average hue.

$$y = 0.0015\ln(x) + 0.0036 \quad (18)$$

$$y = -0.0072x^2 + 0.0096x - 0.0004 \quad (19)$$

Where y is approximate concentration and x is average saturation.

$$y = 0.6091x^2 - 1.1641x + 0.5573 \quad (20)$$

$$y = 0.8597x^2 - 1.6397x + 0.7828 \quad (21)$$

Where y is approximate concentration and x is average value.

3.4 Experimental Analysis

The experimental wells were analyzed for concentration via the MatLab® image analysis code. The code outputted the approximate concentration values as found by mean hue, trimmed mean hue, mean saturation, and trimmed mean saturation. The percent difference data from mean saturation is displayed in Table 5. The percent difference table for mean hue, trimmed mean hue, and trimmed mean saturation are located in Appendix C.

Expected Concentration (g/ml)	Mean Saturation Observed Concentration %	Trimmed mean Saturation Observed Concentration %
0.002	8.5	7.5
0.001818	7.4	6.7
0.00167	4.2	4.8
0.00154	5.0	4.4
0.00143	3.5	4.5
0.00133	8.0	8.3
0.00125	8.8	9.6
0.001176	9.1	12
0.00111	13	12
0.00105	6.8	13

Table 5: Percent difference of observed to expected concentration obtained from mean and trimmed mean saturation

Each of the ten experimental treatments was plotted against the calibration curve in Figure 23. Value produced a plot with values scattered, after this point it was evident value was not a contributing factor for this study and therefore, no longer analyzed. Figure 24 plots the target concentrations of the experimental treatments and the observed concentrations for each dilution. Appendix D displays the standard deviations of the experimental concentration outputs.

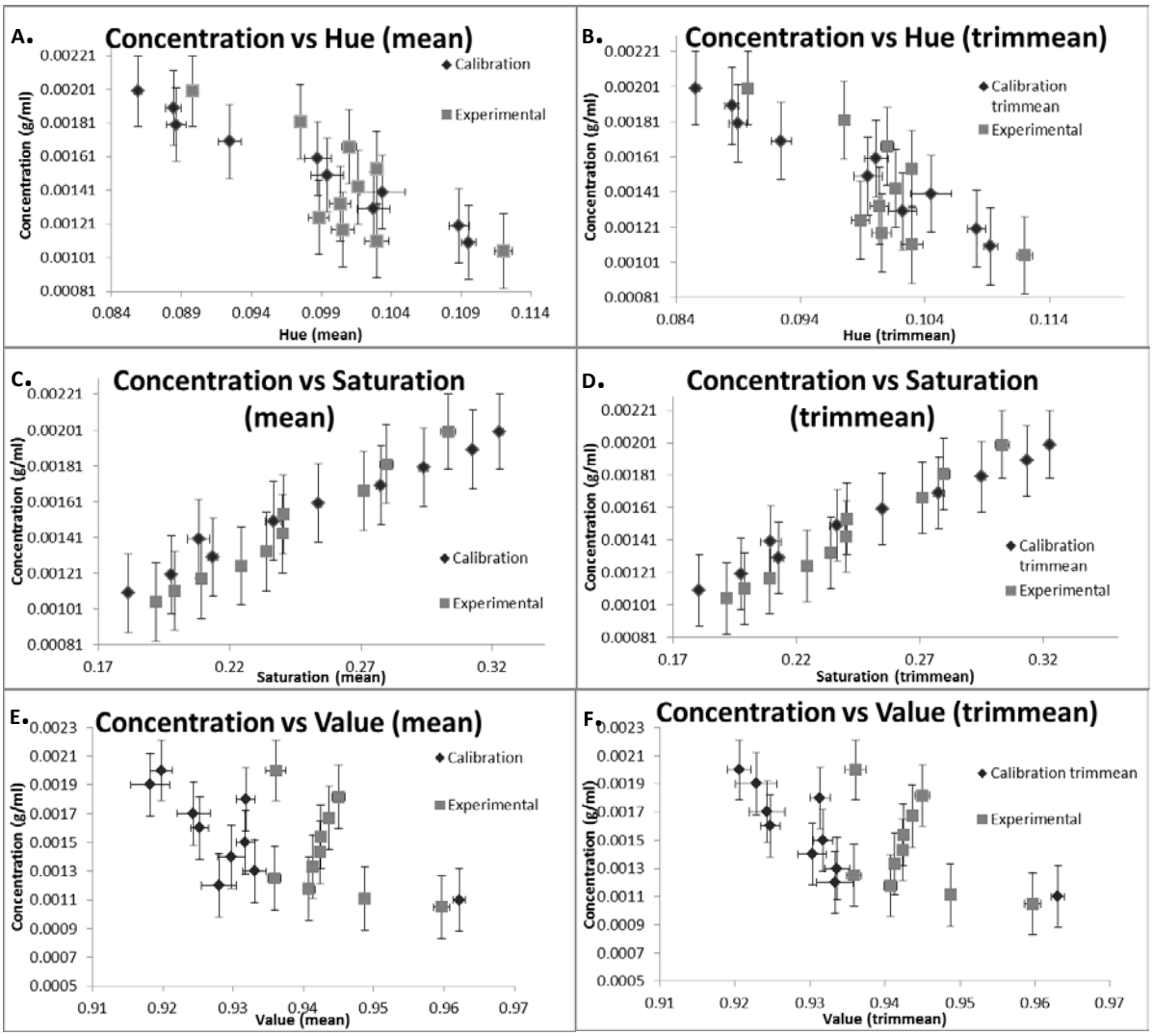

Figure 23: Plots of concentration vs. HSV comparing the calibration to experimental values. A. concentration vs. mean hue B. concentration vs. trimmed mean hue C. concentration vs. mean saturation D. concentration vs. trimmed mean saturation E. concentration vs. mean value F. concentration vs. trimmed mean value.

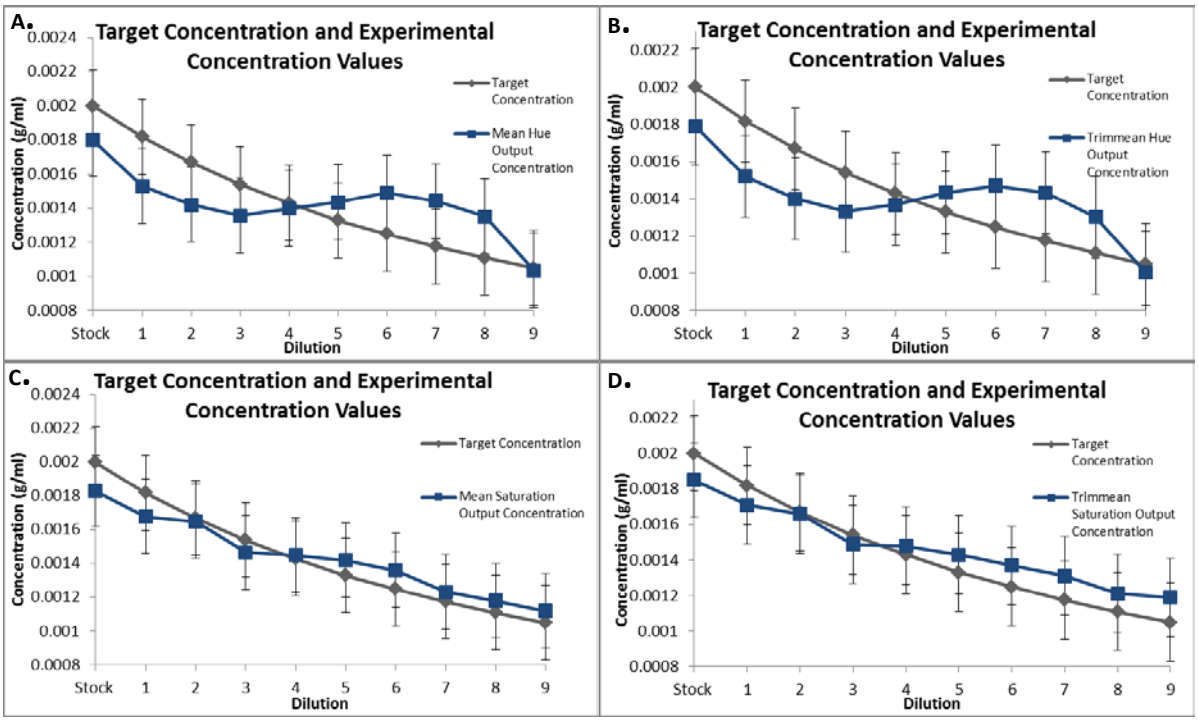

Figure 24: Target concentration and experimental concentration comparison plots. A. mean hue output B. trimmed mean hue output C. mean saturation output D. trimmed mean saturation output.

3.5 Spot Check of Experimental Analysis

The spot check experiment was analyzed via the image analysis code. The results are summarized in Figure 25. Figure 25 plots the target concentration of the treatments with the observed concentration for each dilution. Figure 26 compares the spot check observed concentration with the previous experimental concentration and the target concentration. Appendix E displays the standard deviation of the outputted concentration values analyzed from the spot check.

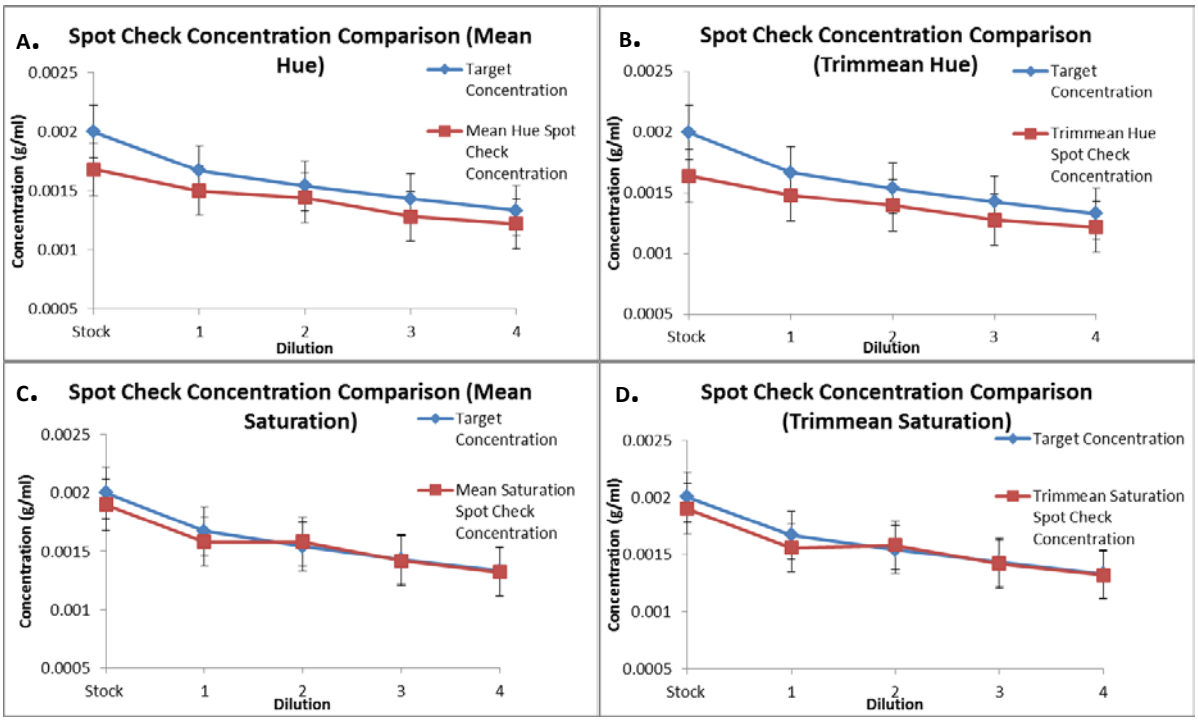

Figure 25: Spot check concentration comparison plots A. mean hue output B. trimmed mean hue output C. mean saturation output D. trimmed mean saturation output.

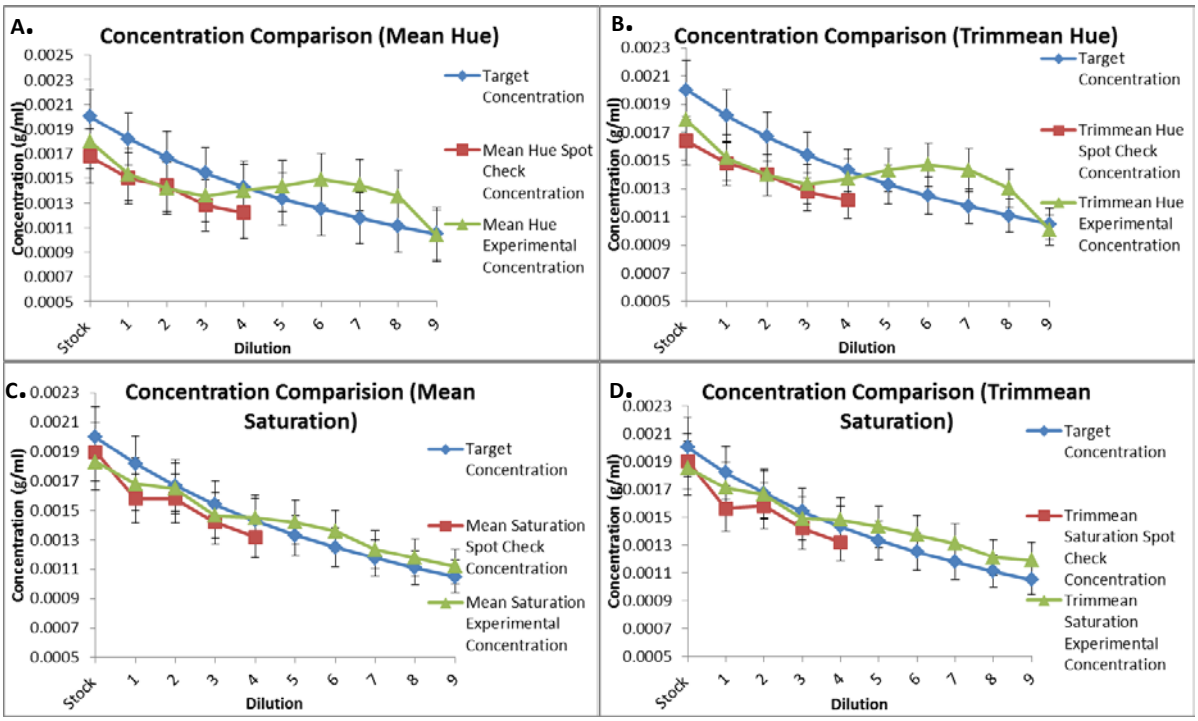

Figure 26: Concentration comparison plots between target, spot check and experimental concentrations A. mean hue output B. trimmed mean hue output C. mean saturation output D. trimmed mean saturation output.

Table 6 presents the percent difference between the target concentration and the outputted concentration from mean hue, mean saturation, trimmed mean hue, and trimmed mean saturation.

Target Concentration	Mean Hue Spot Check Concentration % Difference	Mean Saturation Spot Check Concentration % Difference	Trimmed mean Hue Spot Check Concentration % Difference	Trimmed mean Saturation Spot Check Concentration % Difference
0.002	17.4	5.13	19.8	5.13
0.00167	10.7	5.54	12.1	6.81
0.00154	6.71	2.56	9.4	2.56
0.00143	11.1	0.7	11.1	0.7
0.00133	8.63	0.78	8.6	0.75

Table 6: Percent Differences between target concentration and observed concentrations

4. Discussion

4.1 Discussion

The cross check resulted in three comparison RGB graphs (Figure 20). Due to the fact that the curve fits and error bars overlap, it was determined that the RGB results were within the experimental error of the two programs; MatLab® and ImageJ. RGB value outputs produced a red average percent difference of .325%, blue average percent difference of .187% and a green average percent difference of .997%. This allowed the study to move forward with confidence in the data outputted from the MatLab® image analysis code.

The limit of detection experiment results are summarized in Table 4. Due to the HSV properties summarized in the introduction, it is expected that hue and saturation will get closer to zero as concentration decreases and that value will get closer to one. Table 4 shows that the HSV values bounced around at the lower concentrations, but saturation was the only factor that went from a positive to a negative percent difference and remained negative. This led to the conclusion that the limit of detection can be determined using saturation. For this experiment and under the specific laboratory conditions of this study the limit of detection was concluded to be a concentration of approximately $2.50e^{-5}$ g/ml. Although past this concentration the image analysis code continued to output HSV values, the values were scattered and would pass below the observed baseline.

Figure 16A displays that at concentrations of 0.000192 and 0.000187 g/ml the sample is barely visible and appear as though there is not any sample present, but the image capture and analysis advises that there is. Therefore, it seems as though the image and analysis are more sensitive than the unaided human eye.

The purpose of the calibration was to establish equations from curve fits in order to solve for approximate concentration. Figure 21 A-D display trends whereas E and F are scattered. Trend lines were plotted to obtain line equations (Figure 22). Where the y variable is concentration and the x variable is average hue, saturation, or value as outputted by the image analysis code. The hue trend lines produced R^2 values of approximately 95% and saturation R^2 values of approximately 98%. Value produced an R^2 value of approximately 70%. Therefore, the equations obtained from hue and saturation curve fits were inputted into the image analysis code to solve for approximate concentration. Due to the R^2 values in Figure 22 A-D equations obtained from mean hue, trimmed mean hue, mean saturation and trimmed mean saturation were used in the subsequent experiments to determine which curve fit would produce superior results.

The next goal was to use the image analysis code to determine approximate concentration. This was tested by the experimental well analysis.

From the concentration values obtained and compared to the target concentration it was found that mean hue's concentration output had an average percent difference from the target concentration of 17.04 %, trimmed mean hue's concentration output had an average percent difference of 16.95 %, mean saturation's concentration output had an average percent difference of 7.43 % and trimmed mean saturation's concentration output had an average percent difference of 8.28%. Therefore, mean saturation produced the optimal curve fit for determining concentration. Figure 24's direct comparison of the target and output concentrations also confirms this finding via curve fit and error bar overlap. The concentration results were within the experimental error of the expected result.

It was then necessary to validate the experimental analysis; a spot check was performed for this purpose. A new stock solution was prepared to validate the preparation. From concentration values obtained compared with the target concentration it was found that mean saturation had an average percent difference from the target concentration of 2.94% and trimmed mean saturation had an average percent difference of 3.19%. Again, mean saturation was the optimal curve fit for determining concentration. This confirms the result from the experimental analysis, that mean saturation is the optimal curve fit. Intuitively this makes sense, because the dilutions are altering the shade of red/orange and shade of color is what saturation is most sensitive to. The concentration results were within the experimental error of the expected results.

Replication feasibility was shown by analyzing the concentration of each dilution ten times and then performing the spot check experiment. The spot check was performed using a separate stock solution. Figure 23 and 26 demonstrate that the concentration results were within the experimental error of the expected result. Appendix D and E present the standard deviations between each group (n=10 for each concentration of the experimental and n=5 for each concentration of the spot check) of outputted concentration values.

4.2 Proposed Field Protocol

- Step 1

  Perform lateral flow assay analysis

- Step 2

  Image the result using smart phone device

- Step 3

  Document

  - Smart phone device used
  - Distance image was taken from the test strip (should be around six inches)
  - Luminosity level that the image was taken at

- Step 4

  Email the image of the test strip along with the documented information. If applicable also email a baseline image that will be packaged with the assay.

- Step 5

  Once the lab receives the image and documented information they will run the analysis and from the output determine the diagnosis.

4.3 Conclusion

This study illustrates the capability of a low cost image analysis LFA diagnostic. Although dye was used, the study demonstrated that by calibrating the image analysis code it can be developed to determine color dependent assay results. It was also revealed that the image analysis is more sensitive than the unaided human eye. Possible predictions of the code may include concentration, number of moles, or pH. This work is in response to the need of an available low cost, compact diagnostic. The ability to use resources, such as smart phones and their applications that are readily available will help many people in need of a fast and easy diagnostic.

5. FUTURE WORK

This protocol can be adapted for use with any LFA or LFIA. By using colloidal gold conjugated to antibodies a color specific result will be available. A laboratory may then calibrate the image analysis code to determine a yes or no diagnostic or a diagnostic that is dependent on marker concentration. The specific color can be used to determine if a marker is present in a sample and/or how much of the marker is present.

A limiting factor of this study is luminosity. All images were taken under the same laboratory lighting, but if images were taken in a darker lighting the code's calibration would not be accurate. Fortunately, there are smart phone applications that output luminosity levels. A future calibration should take this factor into account and add another element to the image analysis code of luminosity; therefore, once the analysis is started luminosity could be a selection as smart phone device used for image capture currently is.

Another approach for tackling luminosity would be to include a white baseline card with the packaging of the assay. An image of this card could be taken with the smart phone and sent to the laboratory along with the test strip image and documented information. The analysis can then include analyzing the baseline and use a HSV range to determine which calibration to run the test strip image under.

Furthermore, smart phones have given the user the ability of accessing applications. This code could be adapted into an application. The luminosity could be tested, image taken, and results obtained all within the application on the user's smart phone.

BIBLIOGRAPHY

1. Posthuma-Trumpie, G. A., Korf, J., Amerongen, A., *Lateral Flow (Immuno)Assay: its Strengths, Weaknesses, Opportunities and Threats. A Literature Survey.* Analytical Bioanlytical Chemistry, 2009. 393: p. 569-582.
2. Wang, S., Zhang, C., Wang, J., Zhang, Y., *Development of Colloidal Gold-based Flow-through and Lateral-flow Immunoassays for the Rapid Detection of the Insecticide Carbaryl*. Analytica Chimica Acta, 2005. 546: p. 161-166.
3. Millipore, *Rapid Lateral Flow Test Strips: Considerations for Project Development.* 2008: p. 1-39.
4. Martinez, A. W., Phillips, S. T., Whitesides, G. M., *Three-dimensional Microfluidic Devices Fabricated in Layered Paper and Tape*. Proceedings of the National Academy of Sciences of the United States of America, 2008. 16: p. 19606-19611.
5. Schultz, D. A., *Plasmon Resonant Particles for Biological Detection.* Current Opinion in Biotechnology, 2003. 14: p. 13-22.
6. Sperling, R. A., Gil, P. R., Zhang, F., Zanella, M., and Parak, W. J., *Biological Applications of Gold Nanoparticles.* Chemical Society Reviews,2008. 37: p. 1745-2140.
7. Johne, B., Hansen, K., Mork, E., Holtland, J., *Colloidal Gold Conjugated Monoclonal Antibodies, Studied in the BIAcore Biosensor and the Nycocard Immunoassay Format*. Journal of Immunological Methods, 1995. 183: p. 167-174.
8. Safenkova, I. V., Zherdev, A. V., Dzantiev, B. B., *Correlation Between the Composition of Multivalent Antibody Conjugates with Colloidal Gold Nanoparticles and their Affinity*. Journal of Immunological Methods, 2010. 357: p. 17-25.

9. *Acid Dye.* Encyclopedia Britannica. http://www.britannica.com/EBchecked/topic/3744/acid-dye. (August 2013).
10. *Orange G.* Sigma-Aldrich. http://www.sigmaaldrich.com/catalog/product/sigma/o3756?lang=en&region=US. (August 2013).
11. Abramian, L., El-Rassy, H., *Absorption Kinetics and Thermodynamics of Azo-dye Orange II onto Highly Porous Titania Aerogel.* Chemical Engineering Journal, 2009. 150: p. 403-410.
12. , L. A., Bogatyrev, V. A., Khlebtsov, B. N., Khlebtsov, N. G., *A Protein Assay Based on Colloidal Gold Conjugates with Trypsin.* Analytical Chemistry, 2005. 341: p. 16-21.
13. Fang, S., Tseng, W. Y., Lee, H., Tsai, C., Hou, S., *Identification of Salmonella Using Colony-print and Detection with Antibody-coated Gold Nanoparticles*. Journal of Microbiological Methods, 2009. 77: p.225-228.
14. *What is Photosynthesis.* http://www.dnr.sc.gov/ael/personals/pjpb/lecture/lecture.html. (August 2013).
15. Horvath, H., *Gustav Mie and the Scattering and Absorption of Light by Particles: Historic Developments and Basics.* Journal of Quantitative Spectroscopy and Radiative Transfer, 2009. 110: p. 787-799.
16. Cantrell, K., Erenas, M. M., Orbe-Paya, I., Capitan-Vallvey, L. F., *Use of the Hue Parameter of Hue, Saturation, Value Color Space as a Quantitative Analytical Parameter for Bitonal Optical Sensors.* Analytical Chemistry, 2010. 82: p. 531-542.

17. Kekre, H. B., Sonawane, K., 2012. *Bin Pixel Count, Mean and Total of Intensities Extracted from Partitioned Equalized Histogram for CBIR*. International Journal of Engineering Science and Technology, 2008. 4: p. 1233-1243.

18. Erenas, M. M., Cantrell, K., Ballesta-Claver, J., Orbe-Paya, I., Capitan-Vallvey, L. F., *Use of Digital Reflection Devices for Measurement Using Hue-based Optical Sensors.* Sensors and Actuators B: Chemical, 2012. 147: p. 10-17.

19. Kulp, T. D., Fuld, K., *The Prediction of Hue and Saturation for Non-spectral Lights,* Vision Research, 1995. 35: p. 2967-2983.

20. Capel-Cuevas, S., Cuellar, M. P., Orbe-Paya, I., Pegalajar, M. C., Capitan-Vallvey, L. F., *Full Range Optical pH Sensor Based on Imaging Techniques.* Analytica Chimica Acta, 2010. 281: p. 71-81.

21. *iPhone.* http://www.apple.com/iphone/specs.html (August 2013).

22. Davidovits, P., *Physics in Biology and Medicine.* Elsevier Inc., San Diego. 2008: p. 214-237.

23. Kawamura, S., Tachibanaki, S., *Rod and Cone Photoreceptors: Molecular Basis of the Difference in their Physiology.* Comparitive Biochemistry and Physiology Part A: Molecular & Integrative Physiology, 2008. 150: p. 369-377.

24. Garcia, A., Erenas, M. M., Marinetto, E. D., Abad, C. A., Orbe-Paya, I., Palma, A. J., Capitan-vallvey, L. F., *Mobile Phone Platform as Portable Chemical Analyzer.* Sensors and Actuators B: Chemical, 2011. 156: p. 350-359.

25. Martinez, A. W., Phillips, S. T., Carrilho, E., Thomas, S. W., Sindi, H., Whitestides, G. M., *Simple telemedicine for developing regions: camera phones and paper-based*

microfluidic devices for real-time, off-site diagnosis. Analytical Chemistry, 2008. 80: p. 3699-3707.

26. Cadle, B. A., Rasmus, K. C., Varela, J. A., Leverich, L. S., O'Neill, C. E., Bachtell, R. K., Cooper, D. C., *Cellular Phone-based Image Acquisition and Quantitative Ratiometric Method for Detecting Cocaine and Benzoylecgonine for Biological and Forensic Applications.* Substance Abuse Research and Treatment, 2010. 4: p. 21-33.
27. You. D., Park, T., Yoon, J., *Cell-phone-based Measurement of Tsh using Mie Scatter Optimized Lateral Flow Assays.* Biosensors &Bioelectronics, 2013. 40: p. 180-185.
28. Breslauer, D. N., Maamarri, R. N., Switz, N. A., Lam, W. A., Fletcher, D. A., *Mobile Phone Based Clinical Microscopy for Global Health Applications.* Plos One, 2009. 4
29. Sural, S., Qian, G., Pramanik, S., *Segmentation and Histogram Generation Using the HSV Color Space for Image Retrieval.* IEEE, 2002. 2: p. 589-592.
30. Jeong, S., *Histogram-Based Color Image Retrieval.* 2011 http://scien.stanford.edu/pages/labsite/2002/psych221/projects/02/sojeong/. (August 2013).
31. Konttuir, V., Silfsten, P., Raty, J., *On Optical Properties of Dilute Colloidal Gold.* Plasmonics, 2011. 6: p. 345-349.
32. Liua, X., Xianga, J., Tanga, Y. B., Zhanga, X., Fua, Q., Zoua, J., Linb, Y., *Colloidal gold nanoparticle probe-based immunochromatographic assay for the rapid detection of chromium ions in water and serum samples.* Analytica Chimica Acta, 2012. 745: p. 99-105.

33. Badran, H.A., Ali Hassan, Q. M., Al-Ahmad, A.Y., Chassib, A. E., *Laser-induced Optical Nonlinearities in Orange G Dye: Polyacrylamide Gel.* Canadian Journal of Physics, 2011. 89: p. 1219-1224.
34. Rogers, B., Pennathur, S., Adams, J., *Nanotechnology: Understanding Small Systems*. CRC Press, Boca Raton. 2011: p. 247-271

APPENDIX A: MatLab® Image Analysis Code

```
clc;    % Clear command window.


clear;  % Delete all variables.
close all;  % Close all figure windows except those created by imtool.
imtool close all;   % Close all figure windows created by imtool.
workspace;  % Make sure the workspace panel is showing.

uint8 color_image1; %color image
uint8 color_image2; %cropped image
uint8 hsv_image; %converted image

while(1)
intake=input('Select Device Used 0=iphone5, 1=scanner, 2=iphone4,
3=iphone3Gs:');

buffer=pwd; %load file
[file, pathname] = uigetfile('*.jpg','Load Image');
cd(pathname);
color_image1=imread(file);
cd(buffer);
a=size(color_image1,3);

    figure(1) %crop file
    color_image2=imcrop(color_image1);
    imshow(color_image2);
    save color_image2;


RGB =mean(color_image2);
R = mean(RGB(:, :, 1));
G = mean(RGB(:, :, 2));
B = mean(RGB(:, :, 3));

hsv_image = rgb2hsv(color_image2); %conversion from RGB to HSV

image_h = hsv_image(:,:,1); %HSV layer separation
image_s = hsv_image(:,:,2);
image_v = hsv_image(:,:,3);

    figure(2)
    subplot(3,3,1), imshow(image_h), title('Hue Image');
    subplot(3,3,2), imshow(image_s), title('Saturation Image');
    subplot(3,3,3), imshow(image_v), title('Value Image');

    subplot(3,3,4), imhist(image_h);
    subplot(3,3,5), imhist(image_s);
    subplot(3,3,6), imhist(image_v);
```

```
%Components of Histogram
[hueCounts, hueBinValues] = imhist(image_h);
[saturationCounts, saturationBinValues] = imhist(image_s);
[valueCounts, valueBinValues] = imhist(image_v);


% Plot all 3 histograms in one plot.
  subplot(3, 3, 8);
    plot(hueBinValues, hueCounts, 'r', 'LineWidth', 2);
    hold on;
    plot(saturationBinValues, saturationCounts, 'g', 'LineWidth', 2);
    plot(valueBinValues, valueCounts, 'b', 'LineWidth', 2);
    % Make x-axis to just the max gray level on the bright end.
    xlim([0 1]); ___

%Uses any nonzero Counts and Calculates Average
    [rowHCounts]=find(hueCounts);
    ValuesofHueCount=hueCounts(rowHCounts,1);
    ValuesofHueBin=hueBinValues(rowHCounts,1);
    AverageHue=mean(ValuesofHueBin)

    [rowSCounts]=find(saturationCounts);
    ValuesofSaturationCount=saturationCounts(rowSCounts,1);
    ValuesofSaturationBin=saturationBinValues(rowSCounts,1);
    AverageSaturation=mean(ValuesofSaturationBin)

    [rowVCounts]=find(valueCounts);
    ValuesofValueCount=valueCounts(rowVCounts,1);
    ValuesofValueBin=valueBinValues(rowVCounts,1);
    AverageValue=mean(ValuesofValueBin)

%Best Fit Equations Separated by "intake" selection
if intake == 0


       Approximate_Concentration=-0.0658*(AverageHue^2)-
0.0219*(AverageHue)+0.0043
       Approximate_Concentration=0.0015*log(AverageSaturation)+0.0036
       Approximate_Concentration=-
0.2005*(AverageHue^2)+.0045*(AverageHue)+0.003
       Approximate_Concentration=-
0.0072*(AverageSaturation^2)+0.0096*(AverageSaturation)-0.0004
end
choice = menu('Press yes no','Yes','No');
if choice==2 | choice==0
   break;
end
end
```

APPENDIX B: Limit of detection HSV average values

Concentration (g/ml)	Mean Hue	Mean Saturation	Mean Value
$1.18e^{-4}$	.106	.101	.951
$1.00e^{-4}$	.097	.140	.923
$8.00e^{-5}$	.101	.122	.920
$5.71e^{-5}$	.102	.097	.927
$5.00e^{-5}$	.107	.080	.931
$4.00e^{-5}$	.101	.113	.884
$3.33e^{-5}$	.102	.099	.894
$2.86e^{-5}$	.110	.082	.907
$2.50e^{-5}$	.110	.068	.903
$2.22e^{-5}$	.112	.058	.875
$2.00e^{-5}$	.114	.069	.887
0	.096	.075	.923

APPENDIX C: Percent difference between target concentration and observed concentration of experimental well analysis

Expected Concentration (g/ml)	Mean Hue Observed Concentration%	Mean Saturation Observed Concentration%	Trimmed mean Hue Observed Concentration%	Trimmed mean Saturation Observed Concentration%
0.002	10	8.5	10	7.5
0.001818	15	7.4	16	6.7
0.00167	15	4.2	16	4.8
0.00154	12	5.0	14	4.4
0.00143	8.4	3.5	7.5	4.5
0.00133	17	8.0	17	8.3
0.00125	22	8.8	20	9.6
0.001176	26	9.1	25	12
0.00111	29	13	25	12
0.00105	16	6.8	19	13

APPENDIX D: Standard deviation of experimental analysis concentration outputs

Target Concentration (g/ml)	Mean Hue Output	Mean Saturation Output	Trimmed mean Hue Output	Trimmed mean Saturation Output
0.002	$1.25e^{-4}$	$1.42e^{-4}$	$1.20e^{-4}$	$1.35e^{-4}$
0.001818	$1.42e^{-4}$	$1.40e^{-4}$	$1.32e^{-4}$	$1.52e^{-4}$
0.00167	$1.93e^{-4}$	$8.50e^{-5}$	$1.76e^{-4}$	$9.66e^{-5}$
0.00154	$1.42e^{-4}$	$5.00e^{-5}$	$1.22e^{-4}$	$6.01e^{-5}$
0.00143	$1.49e^{-4}$	$5.27e^{-5}$	$1.34e^{-4}$	$6.32e^{-5}$
0.00133	$2.73e^{-4}$	$1.03e^{-4}$	$2.78e^{-4}$	$9.49e^{-5}$
0.00125	$2.51e^{-4}$	$6.99e^{-5}$	$2.54e^{-4}$	$8.23e^{-5}$
0.001176	$2.60e^{-4}$	$1.22e^{-4}$	$2.60e^{-4}$	$9.28e^{-5}$
0.00111	$3.12e^{-4}$	$1.52e^{-4}$	$2.73e^{-4}$	$1.45e^{-4}$
0.00105	$2.15e^{-4}$	$4.22e^{-5}$	$2.36e^{-4}$	$7.38e^{-5}$

APPENDIX E: Standard deviation of spot check concentration outputs

Target Concentration (g/ml)	Mean Hue Output	Mean Saturation Output	Trimmed mean Hue Output	Trimmed mean Saturation Output
0.002	$1.10e^{-4}$	$7.07e^{-5}$	$1.14e^{-4}$	$7.07e^{-5}$
0.00167	$1.41e^{-4}$	$1.09e^{-4}$	$1.79e^{-4}$	$8.94e^{-5}$
0.00154	$8.94e^{-5}$	$8.37e^{-5}$	$1.22e^{-4}$	$8.37e^{-5}$
0.00143	$2.16e^{-4}$	$8.37e^{-5}$	$2.17e^{-4}$	$8.37e^{-5}$
0.00133	$1.09e^{-4}$	$8.37e^{-5}$	$1.09e^{-4}$	$8.37e^{-5}$